WAKE AND DISPERSION MODELS FOR THE EBR-II BUILDING COMPLEX

JAMES HALITSKY

Consultant in Environmental Meteorology, 122 North Highland Place, Croton-on-Hudson, N.Y. 10520, U.S.A.

Abstract—Wind properties measured downwind of the reactor containment structure at the EBR-II complex were found to be in agreement with predictions made with a mathematical wake model that was derived from measurements in the wakes of suspended flat plates in a wind tunnel and modified for the presence of the ground boundary. Simultaneous concentration measurements of a tracer released in the lee of the reactor containment structure were found to be in agreement with the predictions of a mathematical dispersion model that incorporated the wake model in conjunction with atmospheric turbulence properties. The analysis provides insights into the nature and properties of building wakes in the atmosphere, and their influence on dispersion of released material.

1. INTRODUCTION

A mathematical model of atmospheric dispersion of material released near the ground from a building situated among other buildings is needed in the safety analysis of a nuclear power reactor. No such model has gained general acceptance, primarily because experimental data for its development have been lacking.

In 1967 the Environmental Sciences Service Administration (ESSA)[*] conducted a full-scale experiment at the National Reactor Testing Station, Idaho Falls, Idaho (NRTS)[†] to obtain such data. The results of the study were first published in an ESSA semi-annual report (Van der Hoven, ed., 1967) and a more extended article appeared later in Nuclear Safety (Dickson et al., 1969).

The data gathered in the 1967 experiment include downwind concentrations of a tracer released near the ground at the lee wall of the EBR-II reactor building, and mean wind speed and turbulence upwind and downwind of the EBR-II building complex. The published articles contain tables and graphs of wind turbulence parameters, non-dimensionalized concentration isopleths, and the standard deviations σ_y and σ_z of the lateral and vertical concentration distributions. An empirical expression for the growth of σ_y with downwind distance and rms fluctuation of horizontal wind angle is proposed. The articles contain no mention of attempts to create a wake dispersion model or to relate the observed data to the geometry of the building complex.

The purpose of this paper is to present the factual information gathered in the EBR-II experiments, and to offer a synthesis of the observations in the form of equations for the prediction of wake properties and dispersion downwind of the EBR-II complex. It is believed that the equations have general applicability to wakes generated by most building complexes, but it is recognized that they have been derived from one body of data for a single configuration under essentially neutral stability conditions. Therefore, additional research is needed to study the significance of the characteristic lengths that appear in the analysis, and to validate the wake and diffusion models under conditions of low wind speed and extremes of atmospheric stability.

2. PHYSICAL CONFIGURATION OF THE EBR-II COMPLEX

The general topography at INEL is shown in Fig. 1. The EBR-II complex lies near the center of a wide, flat SW–NE valley. The valley wall northwest of the complex is broken by several NW–SE tributary valleys.

Fig. 2 is a plan view of the EBR-II buildings and the instrumentation arrangement used in the field experiment. The tests were conducted in southwesterly winds only. The meteorological towers were arranged along a SW–NE line through the center of the reactor building. The tracer was released near the ground at the northeast side of the containment structure. The samplers were deployed in arcs centered on the center of the containment structure.

Figure 3 is a photograph of the complex, looking slightly north of east. Figs. 4a and 4b are photographs of a 1:96 scale model of the complex in the New York University air pollution wind tunnel (Halitsky et al., 1963), oriented in the same wind direction as in the 1967 field tests.

The buildings in the complex include the containment structure (dome-capped cylinder), a power plant building, two heat exchanger structures, a fuel cycle facility and a number of smaller auxiliary buildings. The building heights range from 4 m to 29 m, the

---

[*] subsequently integrated into National Oceanic and Atmospheric Administration (NOAA).

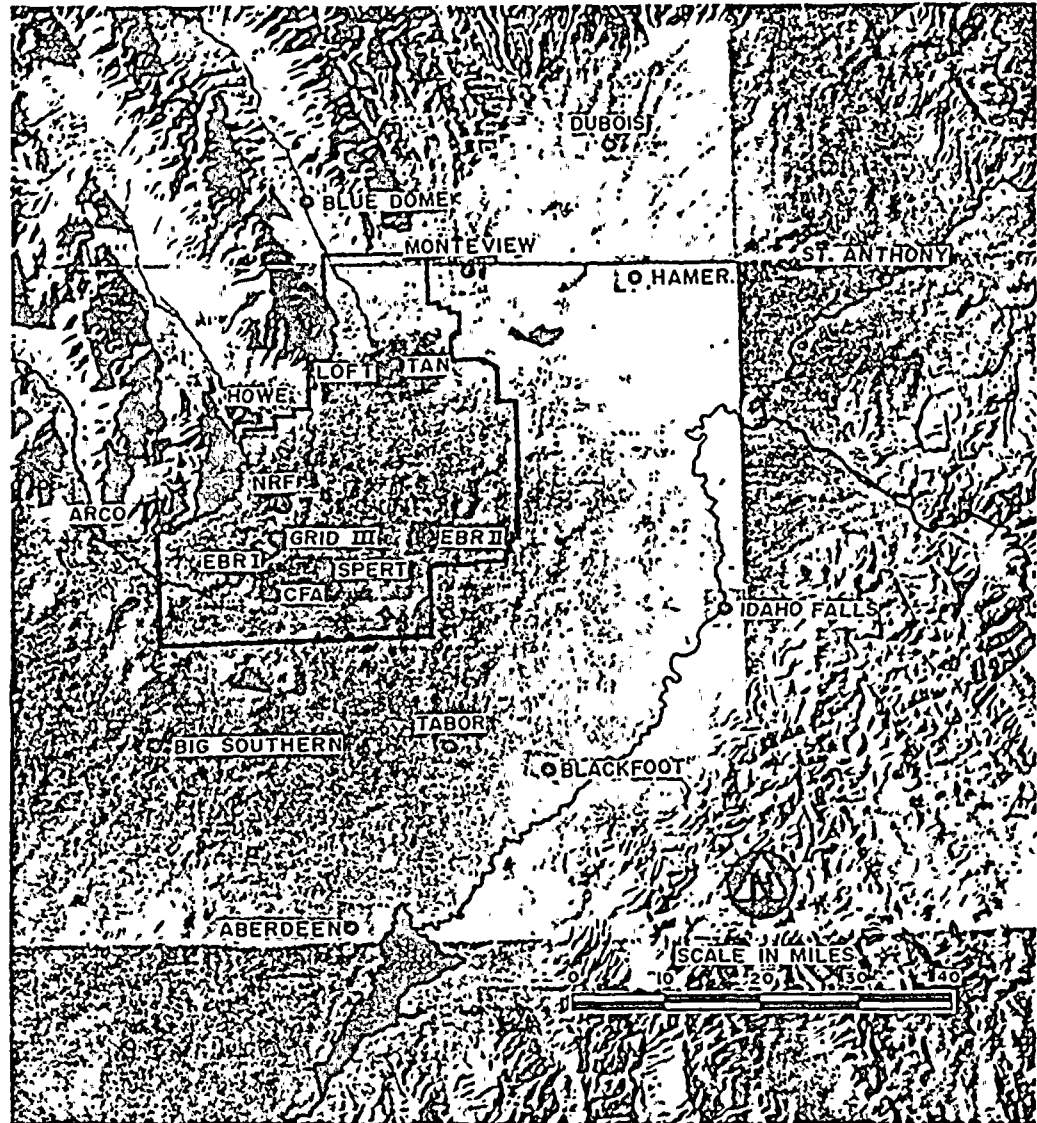[†] subsequently re-named Idaho National Engineering Laboratory (INEL).
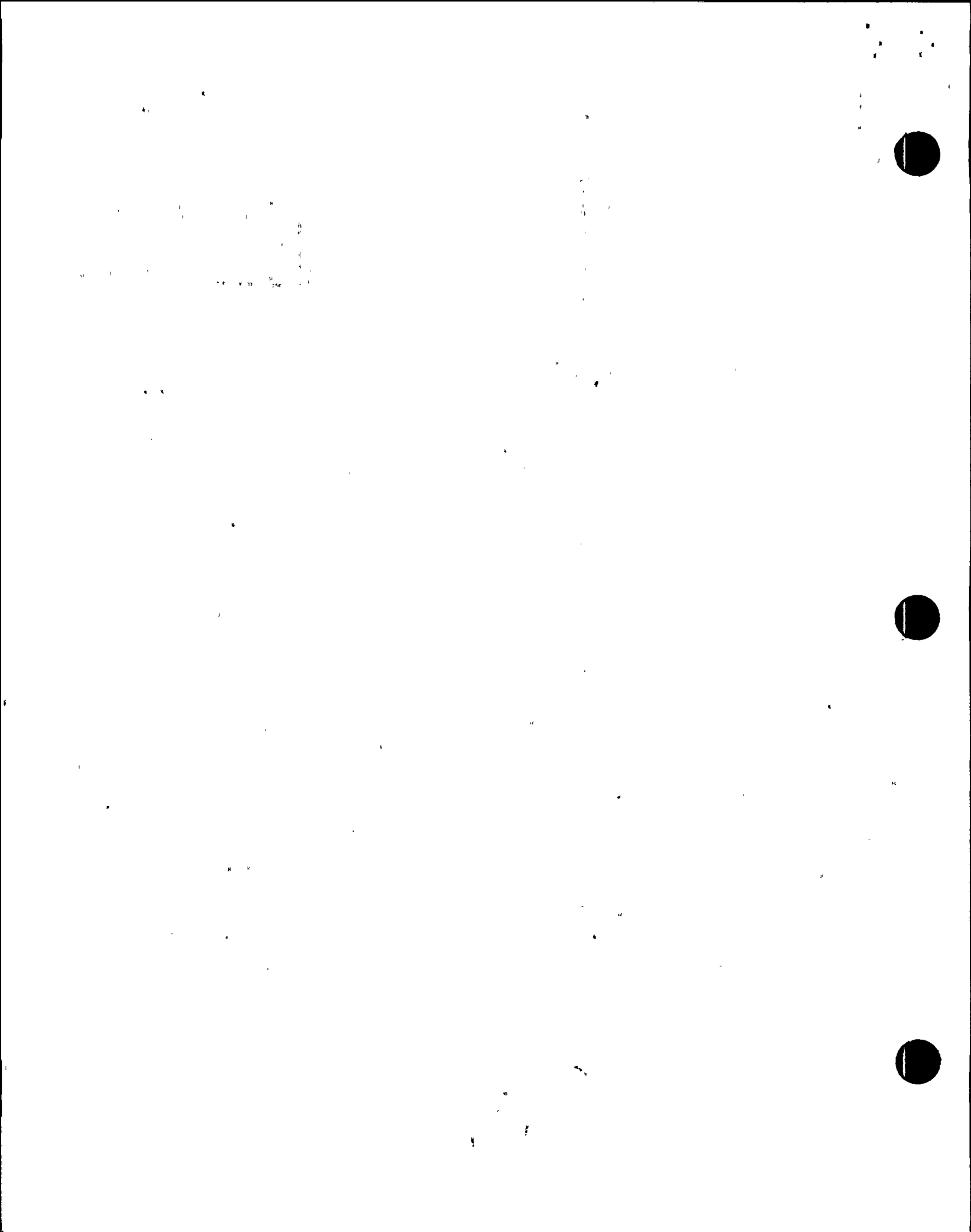
Fig. 1. Terrain at the Idaho National Engineering Laboratory (Source: Van der Hoven, ed., 1968).

highest being the containment structure (29 m) and the power plant building (19 m).

3. DESCRIPTION OF WAKE FLOW

This section is intended to provide the reader with a survey of some aspects of wake flow which will be helpful in understanding the analysis of the EBR-II test data and the development of the dispersion model. Readers who may wish to become more familiar with recent developments in classical wake theory and experimentation as applied to buildings in a boundary layer may consult Counihan et al. (1974) and Castro et al. (1975).

3.1 Definition of Terms

A wake is generally understood to be a region of disturbed flow downwind of an object in a wind stream. It contains a highly turbulent region with cir-culatory flow, called a cavity, immediately in the lee of the object, and a transition region extending some uncertain distance downwind in which the flow properties approach those of the background flow.

Fig. 5 is a sketch of a vertical section through the wake of a solid cube resting on the ground. It shows the background flow, the wake and its cavity, and a displacement zone in which the background flow is accelerated around the cube without substantial change of turbulence.

The cavity boundary in Fig. 5 is a streamline that originates at the building edge (point d) and ter-minates at the downwind stagnation point (point h). In three-dimensional flow, the cavity boundary is a surface that contains all such streamlines. Streamlines that lie within the cavity boundary close upon them-selves to create a toroidal circulatory flow, while the external streamlines continue downwind to re-create the background flow.
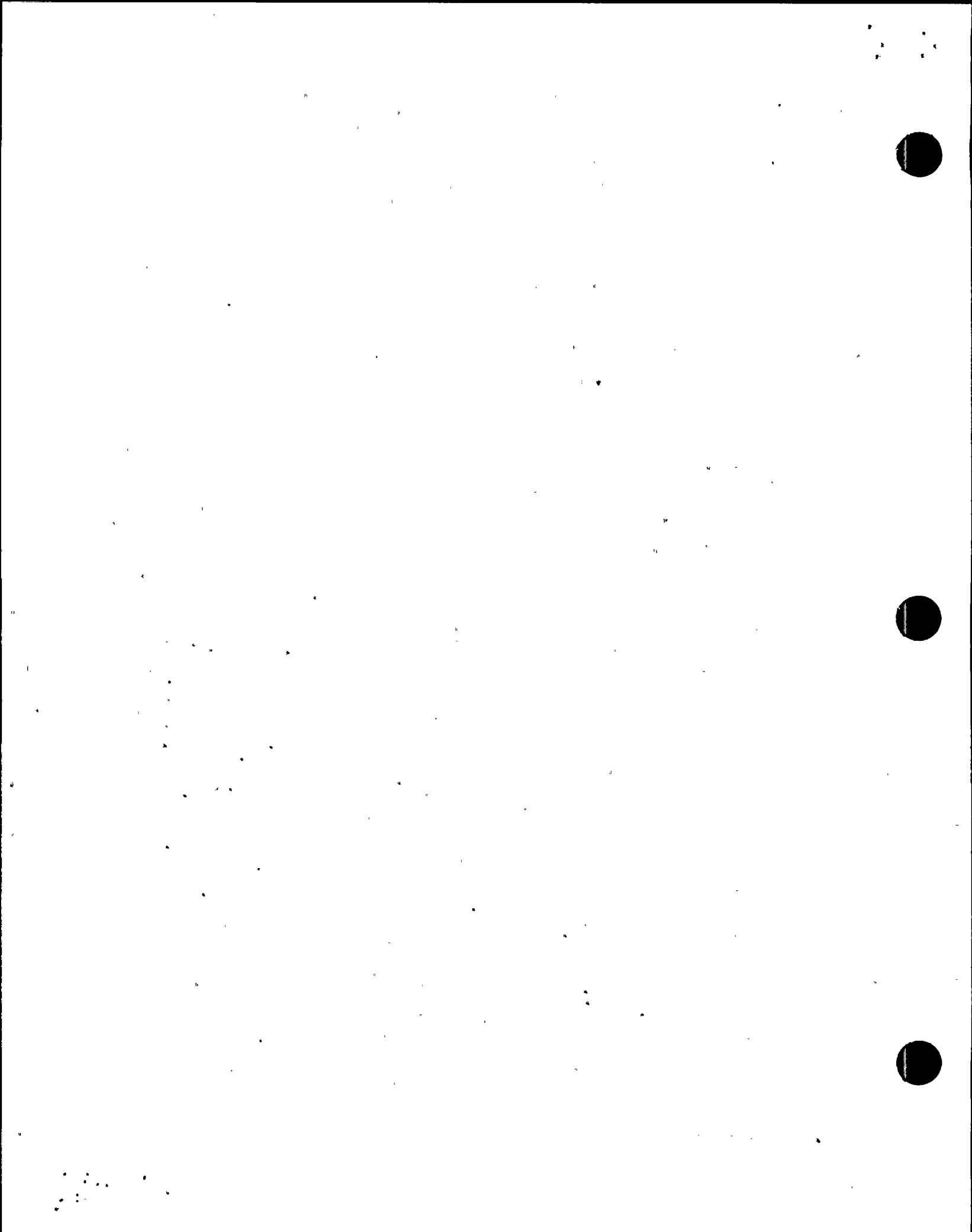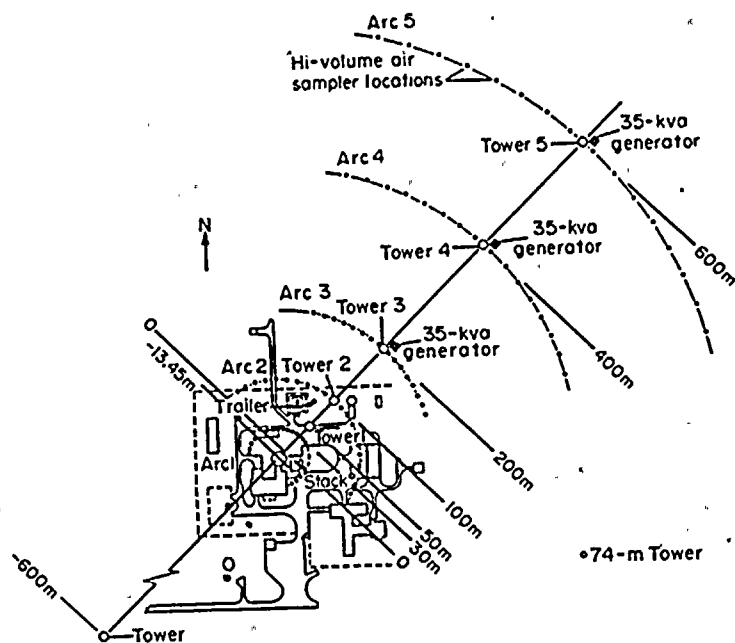
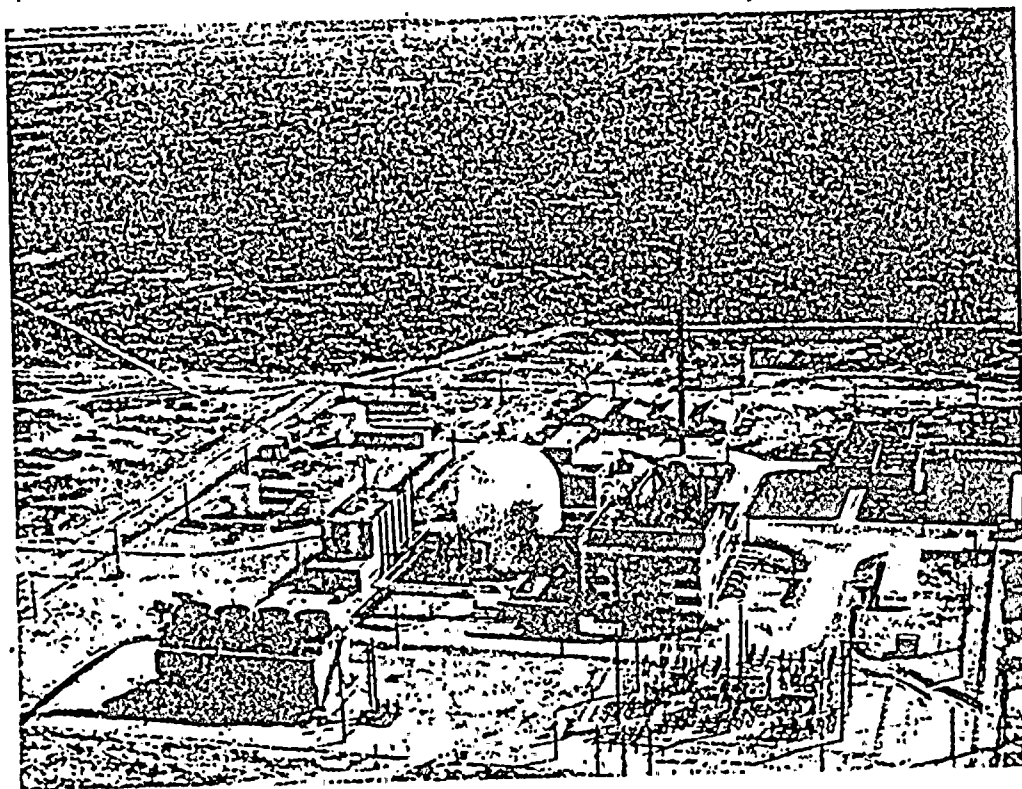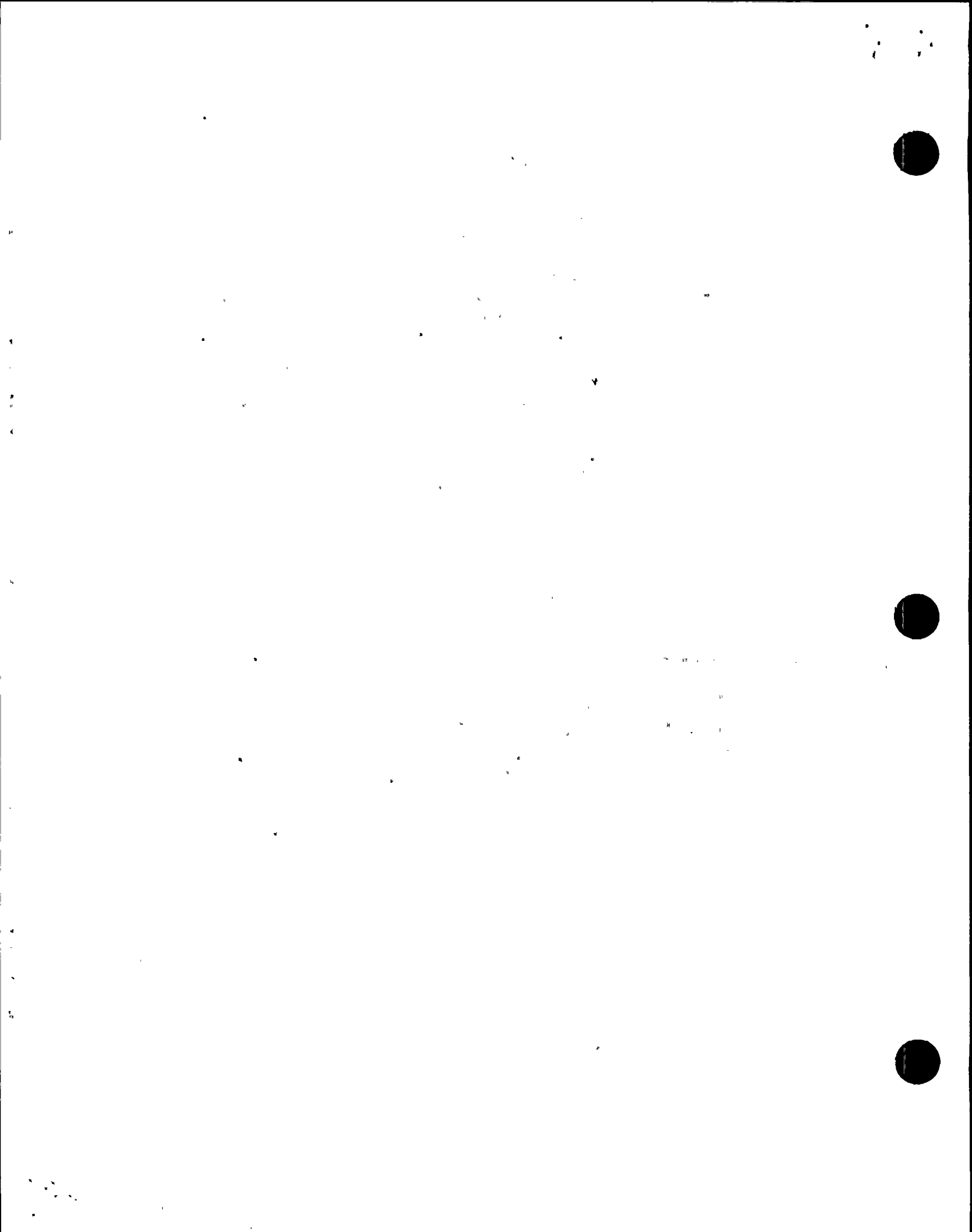Fig. 2. Instrument Locations at the EBR-II Complex (Source: Dickson *et al.*, 1969).

Fig. 3. Photograph of the EBR-II Complex, Looking Slightly North of East (Source: Dickson *et al.*, 1969).
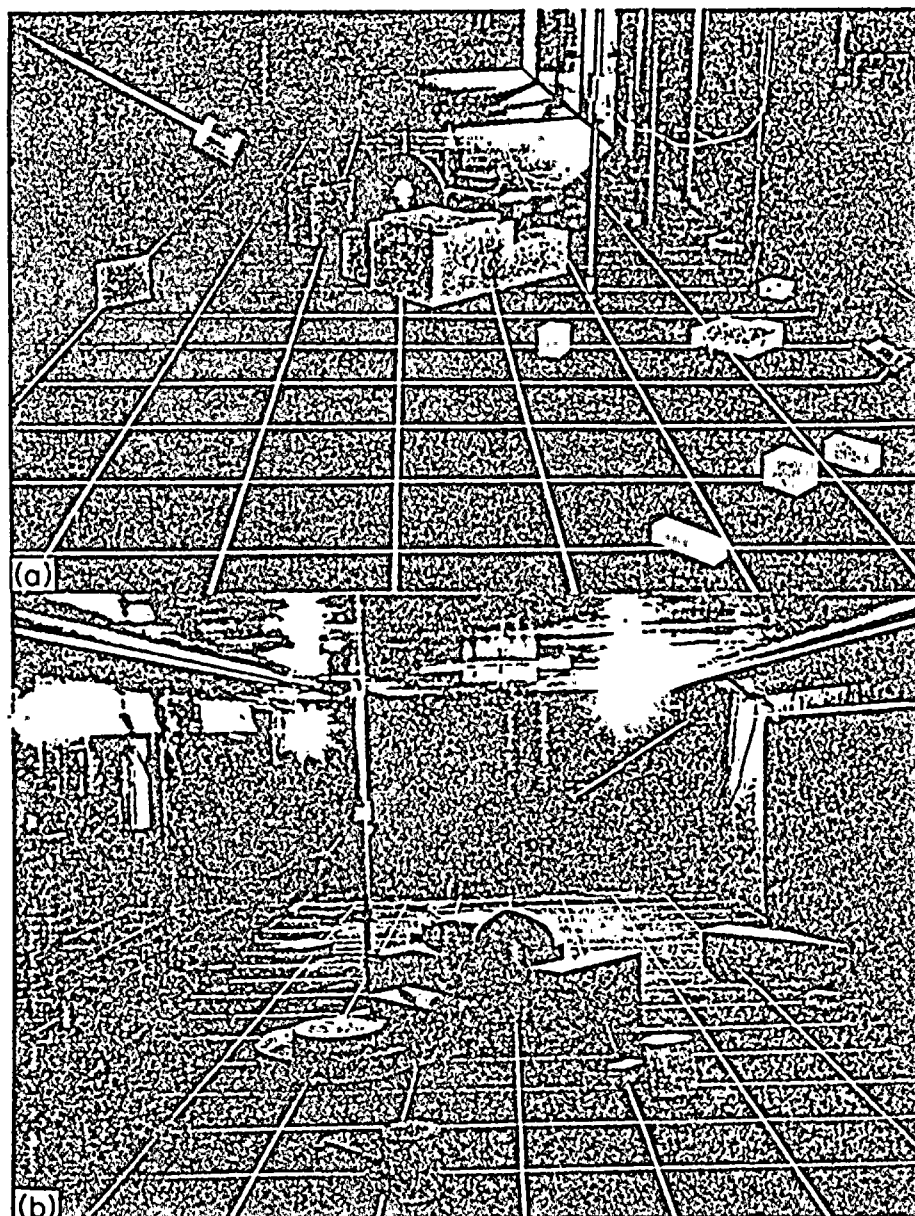
Fig. 4. Photographs of a Model of the EBR-II Complex in the Wind Tunnel. Upper: Looking NE. Lower: Looking SW. Floor markings are 80 ft (24.4 m) squares centered on the containment structure. (Source: Halitsky *et al.*, 1963).

The wake boundary may be defined as the imaginary surface along which the magnitude of a characteristic wake property deviates from that of the background flow at the same location by an arbitrarily small amount. In this paper, two properties will be considered: mean velocity and rms turbulence. Each will provide its own boundary radius, designated $\bar{r}_b$ or r'_b, corresponding to an arbitrarily small deficit of mean velocity or arbitrarily small excess of rms turbulence, respectively.

Since object-generated disturbances decay with radial and downwind distance, the wake boundary as defined above will be a closed surface, perhaps expanding initially as along dmno in Fig. 5, but eventually contracting and terminating.

When several buildings are arranged in a group, each of the buildings will create a wake whose characteristics are dependent on the local background flow for that building. The local background flow, in turn, may be the undisturbed background flow upwind of the group or it may contain flow disturbances created by upwind buildings. If the buildings are closely spaced, as in a building complex, it seems reasonable to expect that the individual building wakes will merge into a composite wake which will be irregular in shape and structure near the buildings, but will acquire the characteristic closed wake boundary and asymptotically developing mean velocity and turbulence distributions at greater downwind distances. The existence of a composite cavity within the com-
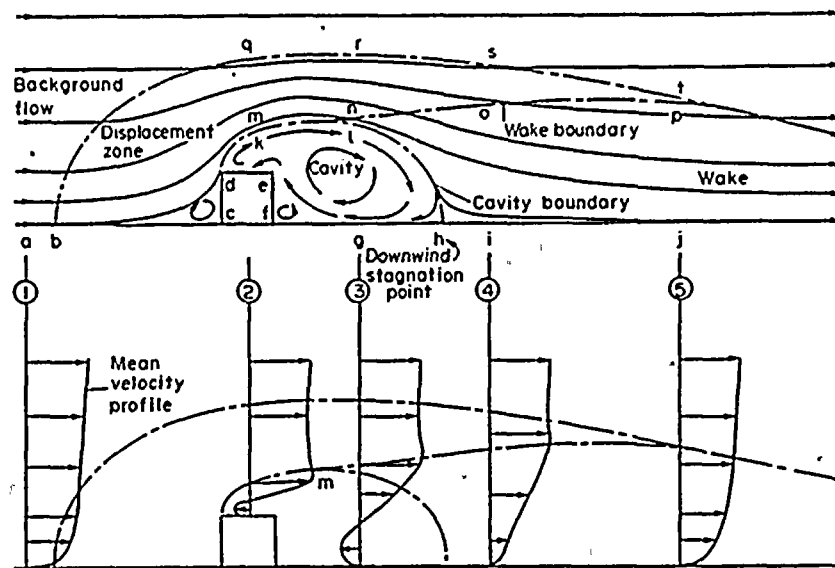
Fig. 5. Sketch of Flow Zones Around a Cube on the Ground (Source: Slade, ed, 1968).

posite wake is probably dependent upon the arrangement of the buildings, since the individual cavities may terminate before they merge.

3.2 Wake Equations

The properties of wake flow that are important to the development of the dispersion model for the EBR-II complex are the longitudinal and transverse variations of mean velocity and turbulence, and the longitudinal variation of boundary radius. In the absence of other data it is proposed to use generalized expressions that are approximations to data measured by Cooper and Lutzky (1955) in the wake of rectangular flat plates suspended normal to an airstream in a low turbulence (0.1%) wind tunnel. Table 1 shows the plate configurations.

It may seem unusual to employ equations that were developed for the wakes of suspended flat plates to describe the wake of a group of buildings on the ground, since the two configurations differ in at least four essential respects. First,. the plates are two-dimensional while the building complex is three-dimensional. Second, the plates are solid while the building complex may be considered porous by virtue of separation of individual buildings. Third, the plates were tested in a uniform stream while the background flow of the complex is a ground surface boundary layer. Finally, transverse gusts are unimpeded as they cross the axis of the plate wake, but they are stopped by the ground surface in the complex wake.

It is, of course, possible to employ physical and mathematical reasoning to estimate the effect of these

Table 1. Flat Plate Test Configurations

Source	Plate Shape	Dimensions (in)	Aspect Ratio R*	Charact. Length L (in)†	Cavity Length x_c/L	Tested Range of x/L min	max
Fail et al. (1959)	Rect.	5.00 × 5.00	1	5.0	2.96	0.6	4.8
	Rect.	3.54 × 7.07	2	5.0	2.86	0.6	4.8
	Rect.	2.24 × 11.20	5	5.0	2.46	0.6	4.8
	Rect.	1.58 × 15.80	10	5.0	2.26	0.6	4.8
	Rect.	1.12 × 22.35	20	5.0	0.96	0.6	4.8
	Rect.	1.24 × ∞	∞	—	2.82‡	0.6	4.8
	Eq. Tri.	side = 7.60	—	5.0	2.82	0.6	4.8
	Circle	dia. = 5.66	—	5.0	2.92.	0.6	4.8
	Tabbed	dia. = 6.00	—	4.3	3.04	0.6	4.8
Cooper & Lutzky (1955)	Rect.	0.2 × 0.2	1	0.20	—	21.0	683
	Rect..	0.2 × 0.6	3	0.35	—	9.1	394
	Rect.	0.2 × 1.0	5	0.45	—	6.9	302
	Rect.	0.2 × 2.0	10	0.63	—	5.5	216
	Circle	dia = 0.2	—	0.18	—	26.4	771

* span/chord.
† (area)$^{0.5}$.
‡ x_c/chord.
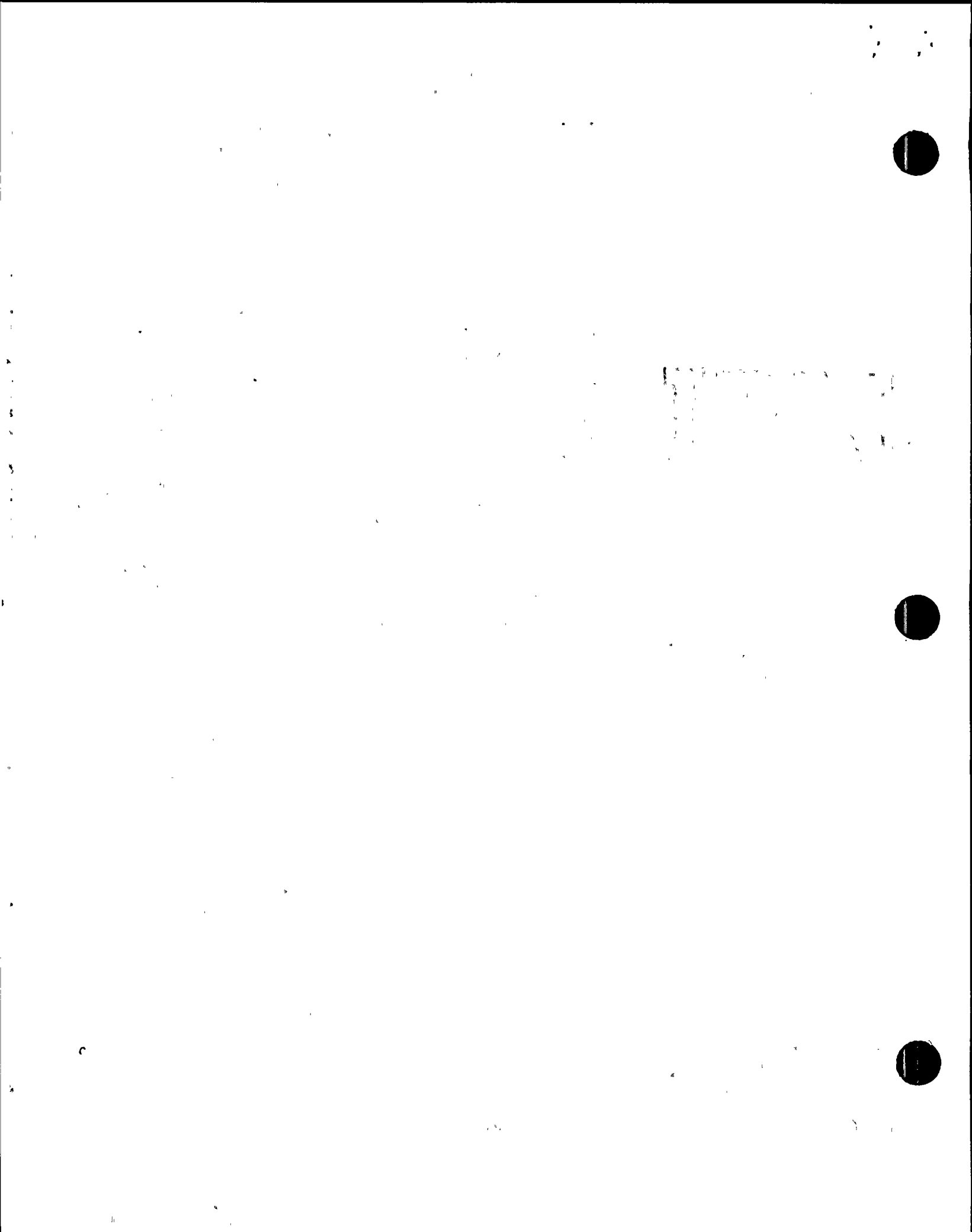
differences, but it is difficult, if not impossible, to validate them with the EBR-II field test data. Accordingly, the equations will be used in the flat plate form, the only adjustments being in the magnitudes of the constants which will be found by comparing the equations with the field test data.

Cooper and Lutzky present their data as graphs of non-dimensionalized flow properties, but they do not generalize the data other than to conclude that the data are in agreement with the theory of axi-symmetric wakes in the following respects:

1. The maximum values of mean velocity defect and rms turbulence vary as (downwind distance)$^{-2/3}$.

2. The radius of the wake varies as (downwind distance)$^{1/3}$.

3. The transverse distributions of mean velocity defect and rms turbulence are universal functions of (radius/wake radius).

The above predictions of wake theory are based on an assumed turbulence-free background flow. Cooper and Lutzky's air stream had small but finite turbulence, and they corrected their measurements by subtracting the turbulent kinetic energy of the background flow. Thus, the data in their paper represent excess turbulence rather than absolute turbulence.

I have fitted curves to Cooper and Lutzky's data, incorporating the above conclusions, and interpreting the turbulence data as excess over background. The equations of the curves are:

Longitudinal Variations

$$(\bar{u}_0 - \bar{u}_a)/\bar{u}_0 = 0.32\,(x/L)^{-2/3} R^{1/5} \qquad (2)$$

$$(\sigma_{u_a} - \sigma_{u_o})/\bar{u}_o = 0.25\,(x/L)^{-2/3} R^{1/5} \qquad (3)$$

$$\bar{r}_b/L = 1.35\,(x/L)^{1/3} R^{-1/10} \qquad (4)$$

$$r'_b/L = 1.80\,(x/L)^{1/3} R^{-1/10} \qquad (5)$$

Transverse Variations

$$\Delta = 1.167 + 0.167 \sin[7.121\,(r/r_b - 0.221)],$$
$$0 \le r/r_b \le 0.441 \quad (6a)$$

$$\Delta = 0.733 + 0.600 \sin[\pi - 5.622\,(r/r_b - 0.162)],$$
$$0.441 \le r/r_b \le 1 \quad (6b)$$

(note: argument is in radian mode)

where:

$\bar{u}$ = longitudinal mean velocity

σ_u = longitudinal rms turbulence

R = plate aspect ratio = span/chord

L = plate characteristic dimension = (chord) $R^{-1/2}$

x = downwind coordinate from plate

r = chordwise coordinate from wake axis

$\bar{r}_b$ = wake boundary coordinate defined ·as the chordwise distance from the wake axis to the point where the mean velocity defect $\bar{u}_o - \bar{u}$ is 10% of the maximum defect at that station

r'_b = wake boundary coordinate defined as the chordwise distance from the wake axis to the point where the rms turbulence excess $\sigma_u - \sigma_{u_o}$ is 10% of the maximum excess at that station

Δ = mean velocity defect ratio, $\bar{\Delta} = (\bar{u}_o - \bar{u})/(\bar{u}_o - \bar{u}_a)$ or rms turbulence excess ratio, $\Delta' = (\sigma_u - \sigma_{u_o})/(\sigma_{u_a} - \sigma_{u_o})$

subscripts

o = background flow

a = on wake axis

b = on wake boundary.

Eqs. 2–5 and the Cooper and Lutzky data are shown in Fig. 6. The dependence on R in Eqs. 2–5 was selected to provide agreement of Eqs. 2–5 with the data at $R = 1$ and $R = 10$. The individual data points in Fig. 6 were obtained from Cooper and Lutzky's faired curves through the transverse distributions. The two upper sets of data points are the curve ordinates at $r = 0$. The two lower sets are the distances to the estimated extension of the faired curves to zero mean velocity defect or zero rms turbulence excess. Some ambiguity may exist in the rms turbulence curves because the extrapolation to zero is a matter of judgment.

Eqs. 6a and 6b describe the transverse distribution of both mean velocity deficit and rms turbulence excess. Fig. 7 shows those equations superimposed on the Cooper and Lutzky mean velocity defect data for $R = 3$ and $R = 5$. The curves match the data at the upwind location ($11 < x/L < 13$), but do not match at the downwind locations where the distribution tends toward Gaussian at $x/L > 220$. Fig. 8 shows the same equations with the Cooper and
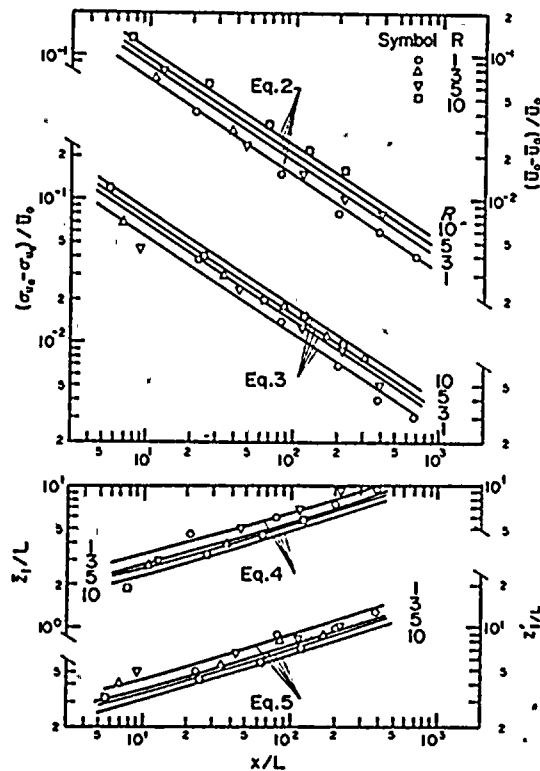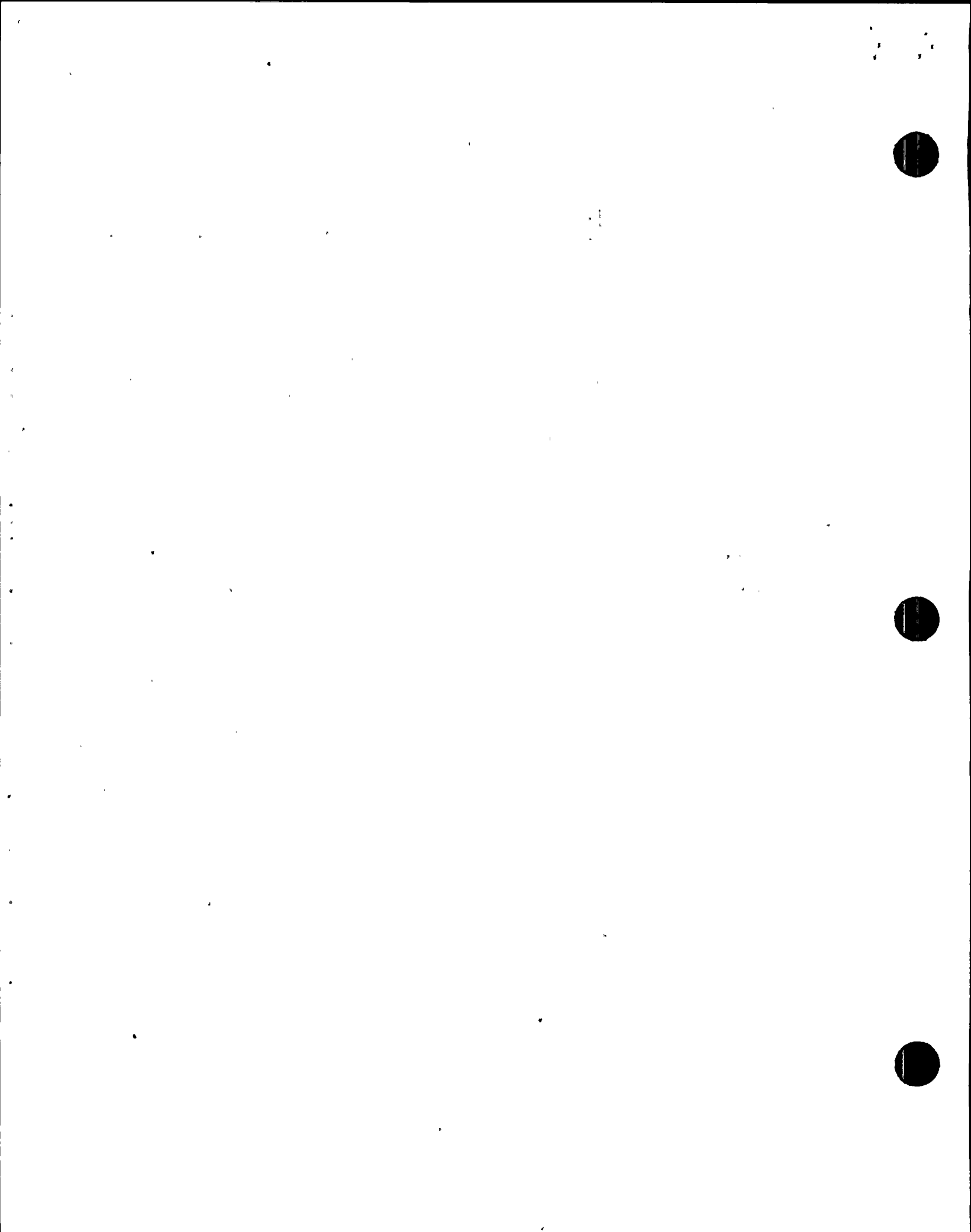

Fig. 6. Properties of Suspended Flat Plate Wakes. Top to bottom: mean velocity defect, rms turbulence excess, wake boundary based on mean velocity defect, wake boundary based on rms turbulence excess.
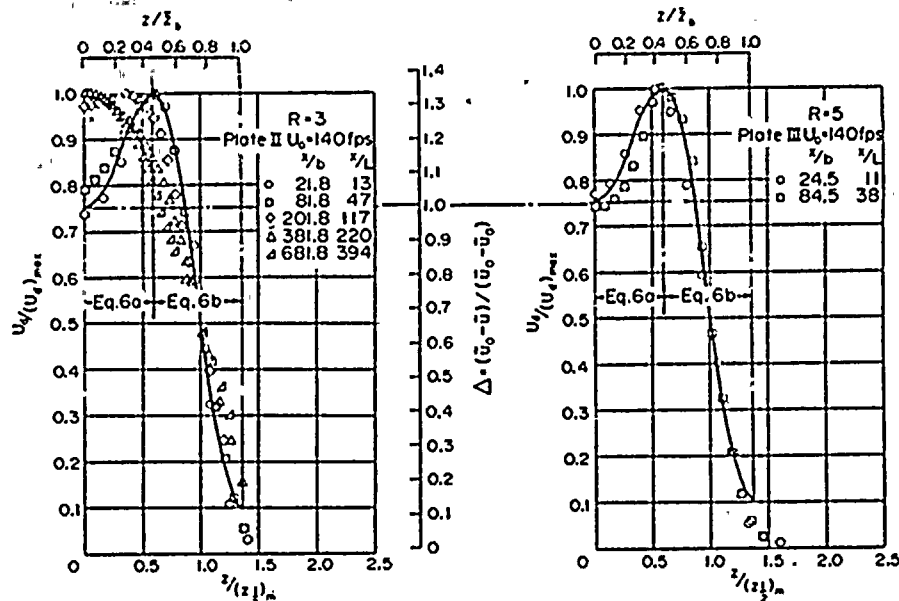
Fig. 7. Normalized Mean Velocity Defect for Suspended Flat Plate Wakes. Left: Aspect ratio = 3. Right: Aspect Ratio = 5. (Source: Cooper and Lutzky, 1955).

Lutzky rms turbulence excess data. The turbulence profile is matched well by the equations in the entire tested range of $7 < x/L < 390$. In both Figs. 7 and 8, the tails of the distributions are not described by the equations, which assume a wake boundary at $r/r_{1/2} = 1.36$. This is the location where the excess or defect is 10% of the peak value or 13.3% of the value at the axis.

It may be noted here that the EBR-II tests were conducted in the range $0.6 < x/L < 6.9$, which corresponds to $50 < x < 600$ m when $L = 87.5$ m. (This value of L is shown in a later section to be character-

istic of the EBR-II complex). Thus, the flat plate test range and the EBR-II test range are coincident with respect to turbulence excess only at the downwind end of the field test range ($x/L \simeq 7$).

Eqs. 2–6 represent measurements taken in the chordwise (parallel to short side) direction, normal to the plate axis. Measurements were not made in the spanwise direction. However, Fail et al. (1955) made complete traverses in the wakes of triangular, circular, tabbed, and square plates in the range $0.6 \leq x/L \leq 3.6$ and found that the wakes had become axi-symmetric at $x/L = 3.6$. Rectangular
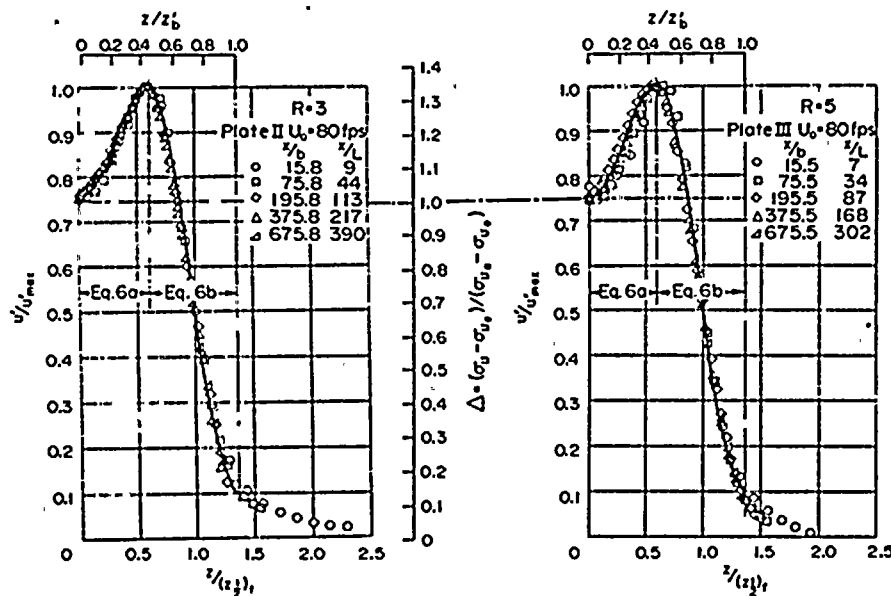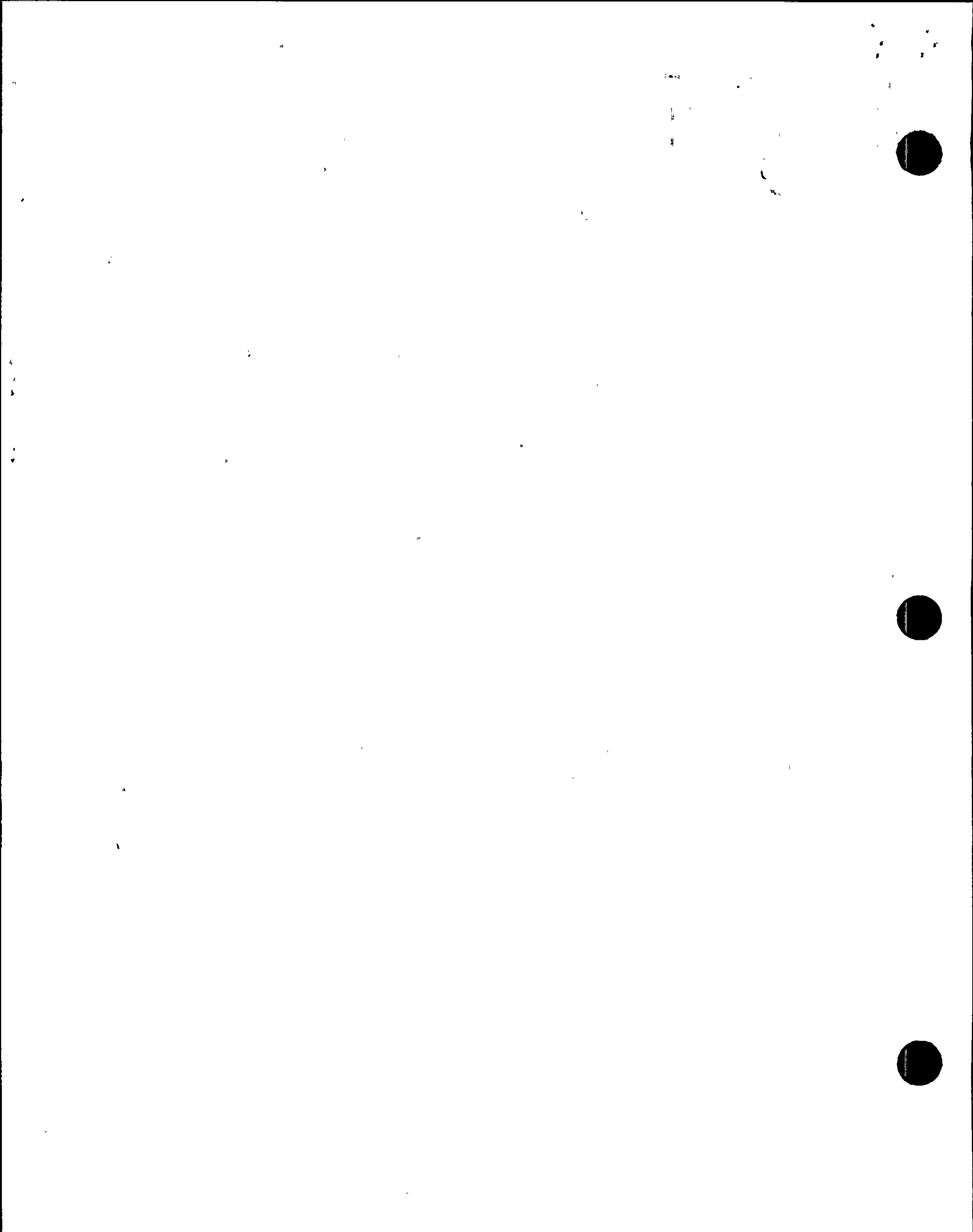

Fig. 8. Normalized R. M. S. Turbulence Excess for Suspended Flat Plate Wakes. Left: Aspect ratio = 3. Right: Aspect ratio = 5. (Source: Cooper and Lutzky, 1955).

plates having aspect ratios between 1 and 10 were found to produce wakes that exhibited essentially the same characteristic. The EBR-II complex has an effective equivalent flat plate in the shape of a rectangle of aspect ratio 3.6 (see later). Accordingly, it does not seem unreasonable to assume that Eqs. 2-6 would be equally valid in the spanwise direction at and beyond the center of the test range.

4. WIND MEASUREMENTS

4.1 Approach Wind Characteristics

Meteorological data taken during the field tests are given in Table 2, which is reproduced from Dickson et al. (1969). The first line of data for each test gives the approach wind condition. All tests were reported to have been conducted in southwesterly winds. The individual mean wind directions were not reported, but the diffusion data in Figs. 3 and 4 of the reference indicate an average wind direction of about 217°.

The Richardson Number was calculated for each test by

$$Ri = (g/T)(dT/dz + \Gamma)(d\bar{u}/dz)_{6m}^{-2} \qquad (7)$$

where

g = gravitational constant = 9.8 m-sec^{-2}
T = 295 K (assumed)
$dT/dz = (T_{74} - T_2)/72$ K-m^{-1}
Γ = 0.010 K-m^{-1} (adiabatic lapse rate).

The value of $(d\bar{u}/dz)_{6m}$ was obtained by assuming a power law for wind speed and taking the derivative at 6 m, giving $(d\bar{u}/dz)_{6m} = nu/6$. Values of the exponent n were assumed to be 0.5 for inversion and 0.25 for lapse temperature gradients. Calculated values of Ri are shown in Table 2. Thirteen of the fifteen tests had $-0.006 \leq Ri \leq +0.004$, indicating near-neutrality. Test 2 was most unstable with $Ri = -0.012$, Test 15 was most stable with $Ri = +0.018$. Even these departures from neutrality are not large.

Table 2. Meteorological Data for EBR-II Site Obtained from 30-min Samples Taken at 6-m Height

Test No.	Date	Time	Tower location	Wind direction standard deviation, deg σ_θ, horizontal	σ_φ, vertical	$\bar{u}$, wind speed, m/sec	ΔT, temp. difference, °C 2–74-m levels at 400-m arc	0.5–2-m levels at 5-m arc	Rich. Number Ri
2	3.1.67	1401–1431	600 m upwind	5.7	3.6	5.1			
			50 m downwind	57.0	16.9	1.8		−0.34	
			100 m downwind	30.5	14.6	2.8			
			200 m downwind	8.9	8.3	4.8			
			400 m downwind	6.2	5.5	4.8	−1.9		−0.012
			600 m downwind	5.8	3.5	5.0			
3	3.7.67	1734–1803	600 m upwind	8.9	4.2	6.0			
			50 m downwind	21.6	11.8	2.0		−0.45	
			100 m downwind	14.2	10.1	4.1			
			200 m downwind	10.9	7.6	5.1			
			400 m downwind	9.1	4.5	6.1	−0.84		−0.001
			600 m downwind	9.0	4.1	6.1			
4	3.7.67	2005–2035	600 m upwind	11.3	3.2	5.8			
			50 m downwind	37.1	13.9	3.3		−0.50	
			100 m downwind	26.6	13.7	3.9			
			200 m downwind	15.2	7.5	4.6			
			400 m downwind	11.8	3.8	5.5	+0.94		+0.003
			600 m downwind	11.1	3.4	5.7			
5	3.8.67	1836–1906	600 m upwind	7.3	3.7	6.0			
			50 m downwind	22.9	10.8	3.5		−0.39	
			100 m downwind	16.4	10.3	4.3			
			200 m downwind	11.1	7.4	5.4			
			400 m downwind	7.3	4.5	6.1	−0.17		+0.004
			600 m downwind	7.2	3.8	6.2			
6	3.8.67	2001–2032	600 m upwind	9.4	3.9	5.7			
			50 m downwind	53.5	14.4	2.8		−0.11	
			100 m downwind	27.9	13.3	3.5			
			200 m downwind	11.0	6.0	5.2			
			400 m downwind	9.4	4.6	5.5	−0.11		+0.004
			600 m downwind	9.3	4.0	5.6			
7	3.8.67	2129–2159	600 m upwind	5.9	3.5	8.0			
			50 m downwind	35.0	16.8	3.7		−0.22	
			100 m downwind	17.6	15.1	5.5			
			200 m downwind	11.4	7.5	5.8			
			400 m downwind	7.2	5.3	7.2	+0.50		+0.001
			600 m downwind	6.0	3.5	8.0			
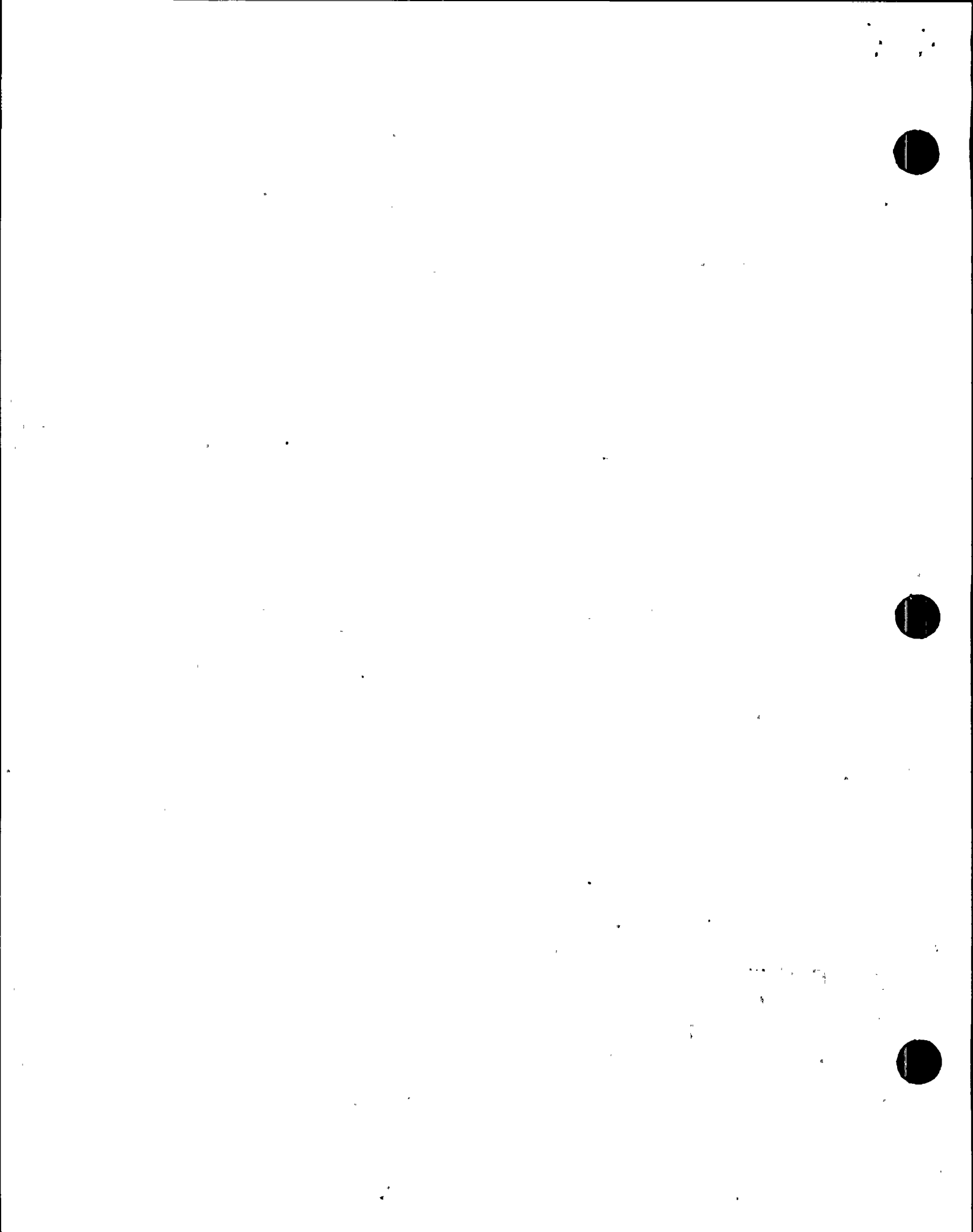
Table 2—continued

Test No.	Date	Time	Tower location	Wind direction standard deviation, deg σ_ϕ, horizontal	σ_ϕ, vertical	$\bar{u}$, wind speed, m/sec	ΔT, temp. difference, °C 2-74-m levels at 400-m arc	0.5-2-m levels at 50-m arc	Rich. Number Ri
8	4.5.67	2027–2057	600 m upwind	8.1	3.9	6.1			
			50 m downwind	17.2	13.2	3.7		−0.28	
			100 m downwind	14.7	12.0	4.3			
			200 m downwind	M*	M*	5.1			
			400 m downwind	8°.1	4.3	5.7	+0.45		+0.002
			600 m downwind	8.0	4.0	6.0			
9	4.5.67	2201–2231	600 m upwind	8.6	4.4	4.2			
			50 m downwind	27.6	11.7	2.2		−0.39	
			100 m downwind	13.9	9.2	2.7			
			200 m downwind	M*	M*	3.1			
			400 m downwind	8.5	4.1	3.8	+0.28		+0.004
			600 m downwind	8.7	4.5	4.0			
10	4.5.67	2332–0002	600 m upwind	6.9	4.3	5.9			
			50 m downwind	15.8	11.1	3.7		−0.34	
			100 m downwind	11.6	9.5	4.3			
			200 m downwind	M*	M*	5.0			
			400 m downwind	6.6	4.2	5.6	+0.39		+0.002
			600 m downwind	6.9	4.2	4.8			
11	4.13.67	1447–1517	600 m upwind	11.9	4.0	9.7			
			50 m downwind	30.9	13.2	5.4		−0.78	
			100 m downwind	19.7	10.9	6.5			
			200 m downwind	11.8	6.7	7.9			
			400 m downwind	10.6	4.0	9.0	−0.28†		−0.006
			600 m downwind	12.1	4.0	9.6			
12	4.13.67	1559–1628	600 m upwind	10.8	4.1	9.8			
			50 m downwind	33.0	12.9	4.7		−0.50	
			100 m downwind	21.9	11.0	6.2			
			200 m downwind	11.4	6.5	8.0			
			400 m downwind	10.9	3.7	9.4	−2.39		−0.005
			600 m downwind	10.9	4.1	9.7			
13	4.13.67	1700–1730	600 m upwind	11.4	3.6	10.5			
			50 m downwind	29.7	13.2	5.5		−0.39	
			100 m downwind	19.8	9.4	6.9			
			200 m downwind	11.0	6.0	8.6			
			400 m downwind	11.5	4.0	9.3	−2.11		−0.003
			600 m downwind	11.5	3.7	10.4			
14	4.13.67	1805–1835	600 m upwind	9.3	4.1	10.3			
			50 m downwind	25.2	11.9	5.0		−0.39	
			100 m downwind	11.3	8.2	6.6			
			200 m downwind	9.4	4.4	7.7			
			400 m downwind	10.2	4.8	7.6	−1.67		−0.002
			600 m downwind	9.4	4.2	10.2			
15	4.13.67	2016–2046	600 m upwind	16.6	2.7	4.0			
			50 m downwind	24.7	12.6	1.7		0.0	
			100 m downwind	20.0	7.9	2.2			
			200 m downwind	16.7	5.4	2.7			
			400 m downwind	19.8	3.8	3.4	+3.72		+0.018
			600 m downwind	16.7	2.8	3.9			
16	4.14.67	1953–2024	600 m upwind	4.6	4.0	6.5			
			50 m downwind	31.2	15.3	2.1		−0.39	
			100 m downwind	18.2	12.4	3.2			
			200 m downwind	9.1	7.6	3.6			
			400 m downwind	6.0	3.6	4.9	+0.56		+0.002
			600 m downwind	4.6	3.9	6.4			

* Data missing.
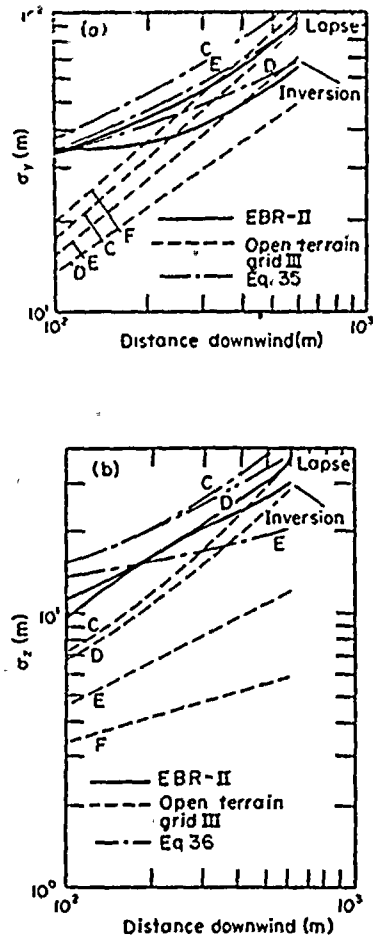† −2.78 according to Van der Hoven, ed. (1967).

Fig. 9. Concentration Standard Deviations at the EBR-II Complex. Top: Lateral. Bottom: Vertical. (Source: Dickson et al., 1969).

' The only unusual item in the approach wind data is the extremely large value of $\sigma_\theta = 16.6°$ in Test 15 under strong inversion conditions. This apparently is a characteristic of the site, as indicated in Fig. 9a by the large values of σ_y in E and F stabilities measured in open terrain west of the EBR-II complex (at Grid III in Fig. 1). A similar enlargement of σ_z does not occur (see Fig. 9b). A possible source of such large perturbations may be density currents created by radiational cooling of the tranverse valley walls northwest of the site, and discharged in a southeast direction into the main valley where the primary flow is from the southwest.

4.2 Wake Characteristics

The test data of Table 2 are graphed in Fig. 10. The portions of the graphs between $x = 50$ m and 600 m are drawn to correct logarithmic scale. Test data are connected by solid lines. The three dashed lines in the σ_θ and σ_ϕ curves between 100 m and 400 m indicate that 'data are missing at 200 m for Tests 8, 9 and 10. Upwind conditions are plotted at the abscissa location marked 600U, and these data

points are connected to the downwind data by dot-dash lines. Horizontal lines extending upwind from 600U and downwind from about 1,000 are intended to represent the undisturbed atmosphere, since the wind properties are assumed homogeneous upwind of the complex, and are assumed to be asymptotic to the same values downwind of the complex.

The ordinate of Fig. 10a is labeled $\bar{u}$ because that is the notation used by Dickson. It should be remembered, however, that speed was measured with a cup anemometer which responds to horizontal winds from any direction. At the downwind end of a wake cavity, where the mean horizontal (vector) velocity is very small, the mean horizontal speed may be appreciably higher because the fluctuating nature of the flow produces continuous wind movement.

The mean speed variation in the lee of the complex is quite similar to that observed downwind of flat plates beyond the cavity region, i.e., low near the cavity and increasing asymptotically to the approach wind value with increasing distance downwind. The minimum recorded speeds occurred at 50 m, at which location the ratio $\bar{u}_{50}/\bar{u}_{600U}$ ranged from 0.32–0.63, with an average of 0.49. The probable existence of smaller speeds upwind of 50 m is indicated by the slopes of the curves. This suggests that a cavity, if one existed, was shorter than 50 m in length. The ratio $\bar{u}_{600}/\bar{u}_{600U}$ ranged from 0.95 to 1.03 with an average of 0.99, indicating that mean speed recovery was substantially complete by 600 m in all tests.

The lateral turbulence intensity $\sigma_v/\bar{u}$, as approximated by the rms horizontal gust angle σ_{θ_a}, is highest at 50 m, and the largest observed value is 57° in Test 2. The slopes of the curves between 50 m and 100 m indicate the probability of higher values at shorter distances. A theoretical maximum value of $360/\sqrt{12} = 104°$ for σ_{θ_a} can occur at the downwind end of a cavity where the distribution of horizontal wind angles may approach uniformity. Thus, the observed variation of σ_{θ_a} is consistent with the hypothesis of a short cavity (<50 m in length).

The vertical turbulence intensity $\sigma_w/\bar{u}$, as approximated by the rms vertical gust angle σ_{ψ_a}, behaves in a similar manner to σ_{θ_a}, with ambient cut-offs at somewhat larger downwind distances because the vertical component of ambient turbulence is smaller than the horizontal component.

The wake boundary cannot be determined from the observed data because no spanwise or vertical distributions of wind angle were measured.

5. MATHEMATICAL DESCRIPTION OF THE EBR-II COMPLEX WAKE

5.1 Fitting of Wake Equations to Observed Data

Numerical values of L and R for the EBR-II complex were found by replacing the complex by an equivalent flat plate implanted in the ground with its center at ground elevation at the tracer release point, its short edges vertical, and its long edges nor-
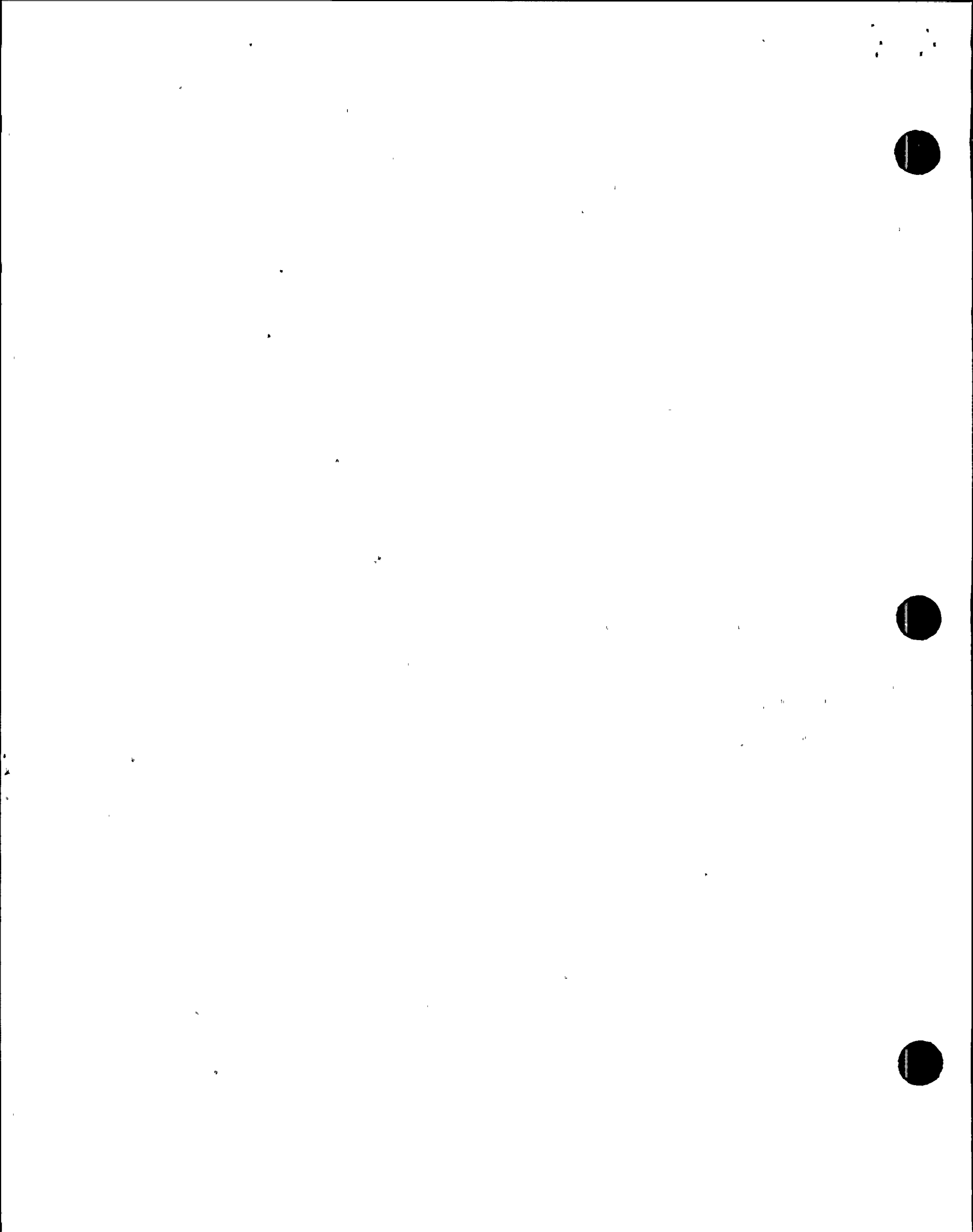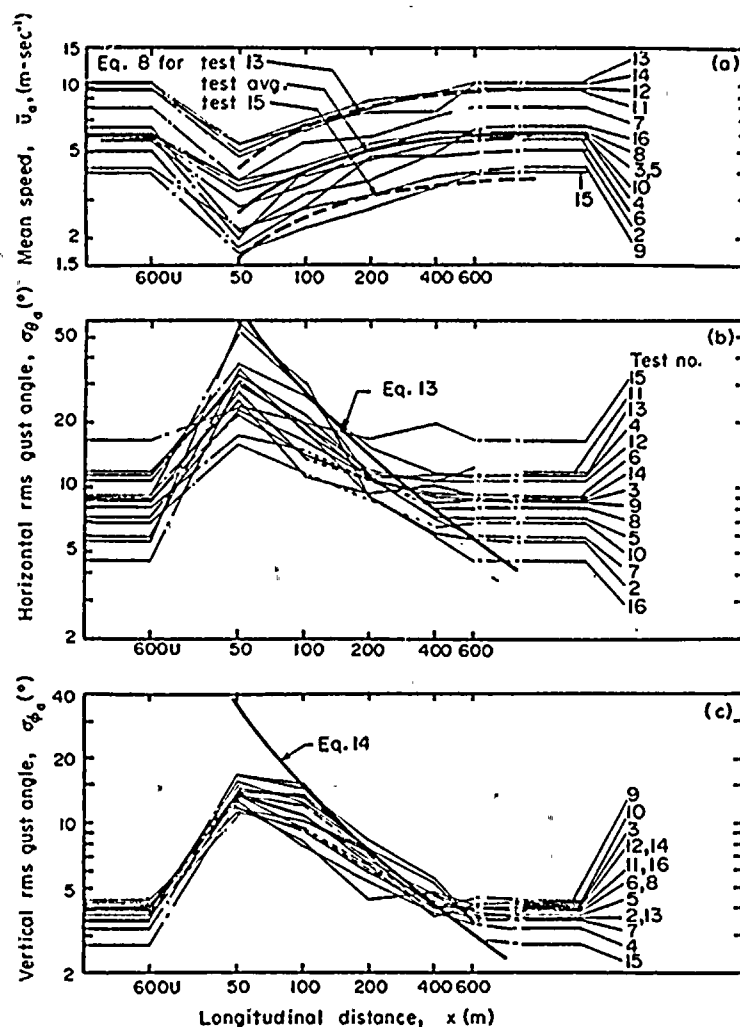
Fig. 10. Wind Properties Along the Line of Towers at the EBR-II Complex. Top: Mean speed. Center: Horizontal gust angle. Bottom: Vertical gust angle.

mal to the wind. The plate is shown superimposed on the complex in Fig. 11.

The exposed half of the plate has height H and width W. Therefore chord $= 2H$, $L = (2H W)^{0.5}$ and $R = W/2H$. Elimination of W from the above yields $L = 2H R^{0.5}$.

A numerical value of H was selected on physical grounds, and a value of L was selected to provide the best agreement of Eqs. 2 and 3 with observed wind measurements. The plate width then followed from above.

The selection of H was based on assuming a plate height which was effectively equal to the average wake height at the center of the complex. Such a wake follows the contour of the containment vessel dome and lies somewhat higher than the roofs of the various other buildings. I chose an average value of $H = 23$ m, which lies between the power plant height of 19 m and the dome height of 29 m.

A trial and error procedure, using Eqs. 2 and 3 and the observations of Fig. 10 led to the selection of $L = 87.5$ m, therefore $R = (87.5/2 \times 23)^2 = 3.618$,

from which $W = 166$ m. Substitution of these values of L and R into Eqs. 2–5 yielded the following downwind equations of an equivalent flat plate wake for the EBR-II complex:

$$\bar{u}_a = (1 - 8.16\,x^{-2/3})\,\bar{u}_o \qquad (8)$$

$$\sigma_{u_a} = 6.37\,x^{-2/3}\,\bar{u}_o \qquad (9)$$

$$\bar{r}_b = 23.4\,x^{1/3} \qquad (10)$$

$$r'_b = 31.2\,x^{1/3}. \qquad (11)$$

Eq. 8 is shown by the heavy lines in Fig. 10a. The solid line represents an average of $\bar{u}_o = \bar{u}_{600U} = 6.6$ m-sec^{-1}. The two dashed lines correspond to the highest and lowest observed values of $\bar{u}_{600U}$, or 10.5 and 4.0 m-sec^{-1}, respectively.

Eq. 9 can be compared to the data in Fig. 10b if the assumption is made that the longitudinal and lateral turbulence intensities are approximately equal, in which case,

$$\sigma_{u_a}/\bar{u}_a \cong \sigma_{v_a}/\bar{u}_a = \sigma_{\theta_a}/57.3. \qquad (12)$$
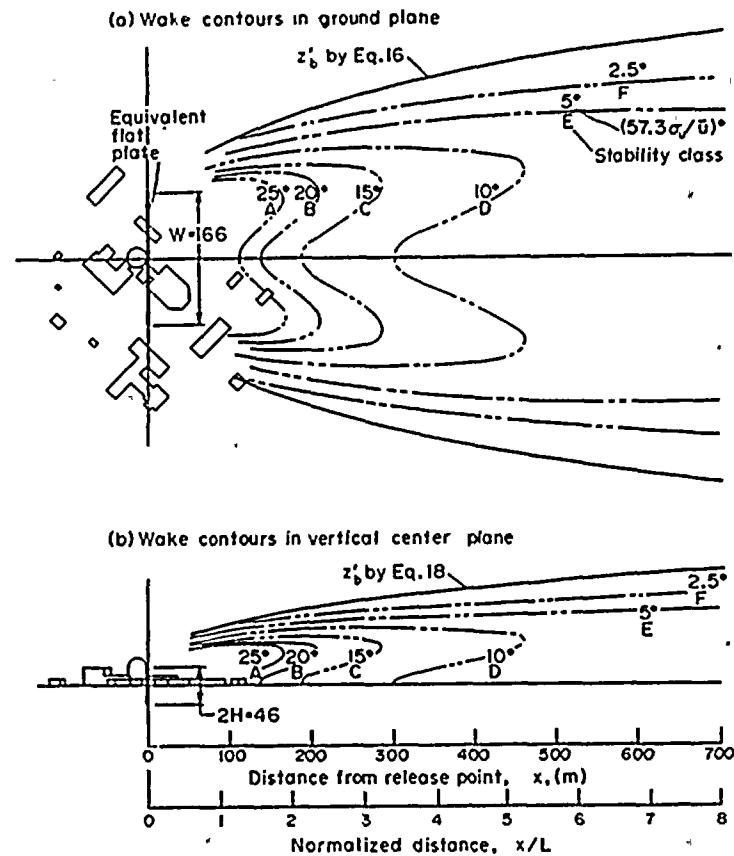
Fig. 11. Calculated Wake Boundaries and Turbulence Intensity Contours. Top: In ground plane.
Bottom: In vertical centerplane.

Combining Eqs. 8, 9 and 12 then yields

$$\sigma_{\theta z} = 365\,(x^{2/3} - 8.16)^{-1}. \tag{13}$$

The heavy line in Fig. 10b is Eq. 13. The predicted values are generally higher than the observations at all distances, but the agreement is better at the longer distances.

Fig. 10c includes a heavy curve that corresponds to the equation

$$\sigma_{\varphi z} = 0.52\,\sigma_{\theta z} \tag{14}$$

where the factor 0.52 is the ratio σ_z/σ_y obtained from Figs. 9a and 9b at a distance of 300 m in D stability, and $\sigma_{\theta z}$ is given by Eq. 13. The rationale for Eq. 14 is that vertical wind fluctuations are suppressed by the ground, whereas longitudinal ones are not. Therefore the approximation analogous to Eq. 12, but for the vertical direction is $\sigma_{\varphi z} = \sigma_{w z}/\bar{u} < \sigma_{u z}/\bar{u}$, and the factor 0.52 is an estimate of the reduction. The 300 m distance and D stability were chosen as an average location and an average stability for the EBR-II tests.

The suppression of vertical turbulence by the ground indicates that the real wake is not axi-symmetric as in the case of the suspended flat plate. It may be inferred, therefore, that the vertical wake boundary is also suppressed. In the absence of other

data, it is proposed that the factor of 0.52 be applied to Eqs. 10 and 11 to yield

horizontal wake boundary

$$\bar{y}_b = 23.4\,x^{1/3} \tag{15}$$

$$y_b' = 31.2\,x^{1/3} \tag{16}$$

vertical wake boundary

$$\bar{z}_b = 12.2\,x^{1/3} \tag{17}$$

$$z_b' = 16.2\,x^{1/3} \tag{18}$$

5.2 The EBR-II Wake in a Turbulent Atmosphere

Figure 11 shows the calculated wake boundary and various longitudinal turbulence intensity contours expressed as the angle $(57.3\ \sigma_u/\bar{u})°$, at the ground plane and in the vertical centerplane, superimposed on plan and elevation views of the complex.

The wake properties in the ground plane in Fig. 11a were calculated by Eqs. 6a, 6b, 8, 9, and 16. By using Eq. 16 rather than Eq. 15 the wake boundary was defined in terms of turbulence excess rather than mean velocity deficit, thereby creating a broader wake. One simplification was introduced to facilitate the computation. The argument in Eqs. 6a and 6b was taken as z/z_b' in the calculation of both Δ' for turbulence excess and $\bar{\Delta}$ for mean velocity deficit.

An exact calculation of $\bar{\Delta}$ would have required the argument to be $z/\bar{z}_v$. This simplification reduced the local mean velocities somewhat, thereby increasing the turbulence intensities and broadening the turbulence intensity contours.

. The wake properties in the vertical centerplane, Fig. 11b, were calculated by Eqs. 6a, 6b, 8, 9 and 18, with the same simplification as used in the ground plane.

The wake as depicted in Fig. 11 is to be interpreted as the wake that would exist at the EBR-II complex if the background flow turbulence were the same as in the flat plate wind tunnel test airstream, and if the turbulence along the wake boundary were in excess of this by some small variable amount. The turbulence intensity along the wake boundary may be found by combining Eqs 2, 3, 6b, 8 and 9 to obtain

$$(\sigma_u/\bar{u})_b = 0.85\,(x^{2/3} - 1.09)^{-1}. \tag{19}$$

This yields values of $(\sigma_u/\bar{u})_b = 0.042$, 0.019 and 0.012 at $x = 100$, 300 and 600 m, respectively. Therefore, at the center of the EBR-II test range the equivalent flat plate boundary turbulence would be about 2%, and the background turbulence would be about 0.1%.

In the atmosphere, the turbulence intensity is larger than in the wind tunnel because friction and temperature differences within the atmosphere generate turbulent eddies whose behavior is customarily categorized by Pasquill stability classes. Slade, ed (1968) suggests that the standard deviation of horizontal wind angle fluctuations, σ_θ, may be taken as an indicator of atmospheric stability. Table 3 contains Slade's values of σ_θ and the corresponding Pasquill stability classes. If the approximation of Eq. 12 is used, it may be seen that turbulence intensity in the atmosphere is not only larger than in the wind tunnel, but it is also larger than at the wake boundary.

The curves marked $(57.3\,\sigma_u/\bar{u})^\circ$ in Fig. 11 may be taken as contours of σ_θ, if Eq. 12 is valid. They may also be viewed as wake boundaries for the specified stability classes when such a boundary is defined as the surface enclosing a region in which the wake turbulence intensity exceeds atmospheric turbulence intensity. This is a crude definition, but it is a useful one for estimating wake boundaries. A more refined definition requires knowledge of the manner in which

Table 3. Atmospheric Dispersion Constants at the EBR-II Site

Pasquill Stability Class	Characteristic σ_θ According to Slade (deg)	(rad)	a_y	p_y	a_z	p_z
A	25	0.436				
B	20	0.349				
C	15	0.262	0.284	0.90	0.064	0.99
D	10	0.175	0.488	0.72	0.120	0.86
E	5	0.087	0.300	0.85	0.403	0.53
F	2.5	0.044				

σ_θ (rad) $\approx \sigma_v/\bar{u}$, $\sigma_y = a_y\,x^{p_y}$, $\sigma_z = a_z\,x^{p_z}$.

atmospheric and wake turbulent energies combine, a subject which needs considerable investigation.

The lobed shape of the curves in Fig. 11 is the result of a peaking of turbulent intensity at $r/r_o' \simeq 0.40 - 0.45$. This peak is produced by the rolling up of vortex sheets generated at the periphery of the complex (or at the edges of its equivalent flat plate). It seems to be a permanent feature of the wake, as may be inferred from Fig. 8. This behavior is markedly different from that of the peak mean velocity defect, which occurs at about the same radial distance in the EBR-II test range, but progresses inward toward the axis with increasing distance downwind, according to Fig. 7.

The curves have not been extended to $x/L = 0$ because the equations do not predict realistic values at short distances. Such deviations may be attributed to the presence of building cavities and, possibly, of a continuous cavity of the entire complex. It may be noted that the cavity of the containment vessel when standing alone would extend to 2.3 diameters or 56 m from the center of the vessel (Frame 14, Fig. 5.23, Slade, ed. (1968)). This corresponds to $x = 43$ m from the release point in the complex. It seems possible that flow re-organization in the lee of the containment vessel cavity could account for much of the deviation between predicted and observed characteristics at short distances, with the remainder due to flow disturbances created by the adjacent buildings.

An important aspect of Fig. 11 is the illustration that wakes are finite in extent, and their lengths vary inversely as the stability (short for unstable, long for stable). The wake of the EBR-II complex in neutral stability (Pasquill D), is about 300 m long at the axis and about 450 m long at the end of the lobe. At the extremes of the stability range, the axial lengths would be about 110 m for Pasquill A and 1910 m long for Pasquill F, according to the model equations. Confirmation of model predictions in other than Pasquill D stability is lacking, but the above estimates should be qualitatively correct, at the least.

6. DISPERSION

6.1 General Properties of Wake Plumes

A plume will be defined as the region containing non-zero concentrations of dispersed material. The plume boundary is the curved surface that encloses all of the released material.

A wake plume is a plume whose source lies within a wake. The boundary of a wake plume may take either of two forms, depending upon the location of the source within the wake. If the source lies within the cavity, material will disperse rapidly to the cavity boundary by cavity circulation and diffusion, then it will disperse to the wake boundary by wake turbulence outside of the cavity, and finally, it will disperse by atmospheric turbulence beyond the wake boundary. The plume boundary for a source in the cavity will extend from the most upwind end of the wake

(point d in Fig. 5, for example) to infinity downwind, and will have a radial dimension which is larger than the wake boundary radius and increases monotonically with distance downwind at a rate that is solely dependent on atmospheric turbulence. The latter characteristic is a consequence of the definition of a wake boundary as the surface beyond which the turbulence is atmospheric.

If the source lies within the wake downwind of the cavity, material will disperse by wake turbulence to the wake boundary and then by atmospheric turbulence beyond the wake boundary. The plume boundary for such a source will extend from the source to infinity downwind, and will have a radial dimension that grows monotonically with distance downwind from the source at a variable rate depending on the local intensity of wake or atmospheric turbulence at the plume boundary.

In the classical approach to diffusion, one usually specifies the spatial distribution of diffusivity and mean velocity, and then proceeds to a solution of the differential equation of diffusion, either in closed form or by numerical approximation. When the diffusivity is constant in a transverse plane, the mathematical solution is a Gaussian distribution of concentration. While the Gaussian distribution is quite realistic for most of the plume region, it is not realistic near the boundary because it predicts that material will be found everywhere out to infinity in a radial direction. In order to overcome this physical impossibility, it is conventionally assumed that the Gaussian distribution is valid to some nominal radial distance, after which the concentration is zero. Frequently, this distance is taken to be $r = 2.5\ \sigma_r$, at which point the concentration is 4.39% of the axial concentration, and the material enclosed within the boundary of a bi-Gaussian plume is 0.987^2 or 97.4% of the released amount.

In wake diffusion, the diffusivity is not constant in a transverse section; therefore the Gaussian distribution is not a good representation, even at interior locations. Until adequate experiments are performed to establish the spatial distribution of diffusivity in wakes, it would seem to be more prudent to employ the plume boundary as a basic parameter in conjunction with concentration distributions that seem reasonable on physical grounds and agree reasonably well with measurements.

Accordingly, the approach that was used in developing the dispersion model for the EBR-II complex was to combine realistic radial concentration distributions, plume boundaries and mean velocity distributions in an equation that satisfied mass continuity and predicted the observed decay of concentration along the plume axis.

6.2 Dispersion Measurements

Dispersion was measured at the EBR-II complex by sampling concentrations of uranine dye released adjacent to the downwind surface of the containment vessel. The sampling grid is shown in Fig. 2. The x axis extended to the northeast, the centers of the sampling arcs were at the center of the containment vessel, and the arcs intersected the x axis at distances of 30, 100, 200, 400 and 600 m from the release point. The release and sampling points were at an elevation of 1 m above ground, and the release and sampling periods were 30 min.

Thirteen tests provided usable data for dispersion analysis. These were Tests 2–13 and Test 16 in Table 2. Seven tests were conducted under lapse conditions and six under inversion conditions; however, the stability was essentially neutral for all except, perhaps, Test 2, because of the high wind speeds.

Discrete concentration measurements are not given in Dickson et al (1969). The data are presented as isopleths of the concentration coefficient K, and graphs of the longitudinal and vertical standard deviations of concentration distribution σ_y and σ_z and centerline concentration X_p vs downwind distance.

The non-dimensional concentration coefficient K is defined by

$$K = X\ \bar{u}_o\ A\ Q^{-1} \qquad (20)$$

where

X = local concentration (g m^{-3})
$\bar{u}_o$ = mean velocity of background flow, assumed to be $\bar{u}_{600v}$ in Table 1 (m – sec^{-1})
Q = release rate (g sec^{-1})
A = a characteristic area for wake dispersion analysis. The Nuclear Regulatory Commission customarily sets A equal to the area of the isolated containment vessel projected onto the y-z plane. For the EBR-II reactor, $A = 665\ m^2$. This was the area used by Dickson et al.

In presenting the data, Dickson et al. grouped the tests according to temperature gradient, i.e., lapse (7 tests) or inversion (6 tests). Isopleths of K_{max}, K_{mean} and K_{min} were given for each gradient group. The K_{mean} isopleths are reproduced herein as Figs. 12 (lapse) and 13 (inversion). The solid curves are the test observations.

The lateral standard deviation of concentration σ_y was computed from the concentration distribution in each arc. Two methods, not explained in detail, were used. The first, apparently, was the conventional statistical treatment of a group of measurements. The second is said to be based on X_p and the crosswind integrated concentration CIC. Fig. 11 of the reference gives the formula

$$\sigma_y = (\text{CIC})(2\pi)^{-1/2}(X_p)^{-1} \qquad (21)$$

where

X_p = peak concentration along an arc

$$\text{CIC} = \int_{-\infty}^{\infty} X\ dy$$

(Note: in reference Fig. 11, X_p is shown under the square root sign but this is believed to be a drawing error).
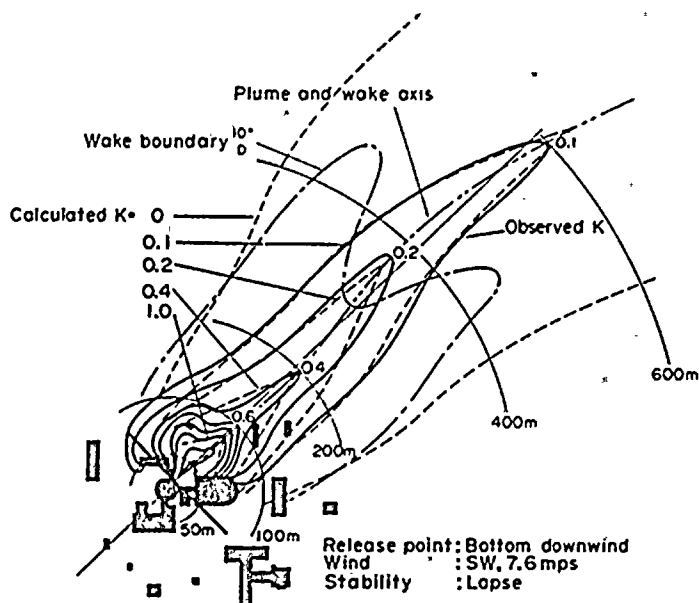
Fig. 12. K-Isopleths in the Ground Plane as Observed (Mean of Lapse Tests) and Calculated for Neutral Stability (Source: Dickson *et al.*, 1969).

The vertical standard deviation σ_z was not measured, but was computed from the lateral distribution of concentration, using the assumption that the vertical distribution of concentration was Gaussian. Presumably, σ_z is given by

$$\sigma_z = Q\,(CIC)^{-1}\,(2\pi)^{-1/2}. \qquad (22)$$

App. A contains derivations of Eqs. 21 and 22.

The observed variation of mean σ_y and σ_z vs x for the two temperature gradient classes is shown in Fig. 9.

The observed variation of centerline concentration with downwind distance for all tests is given in Fig. 10 of Dickson *et al.* However, the source strength is not given; therefore the ordinates cannot be converted to values of K. Dickson *et al.* stated that the power law relationship $X_p \sim x^{-0.6}$ fits the data quite well for both lapse and inversion conditions. The exponent -0.6 is approximately the linear slope of the X_p vs x curves on the log–log plot of Fig. 10, but a correction is needed for the difference in ordinate and abscissa scales. The corrected exponent would be -1.34.
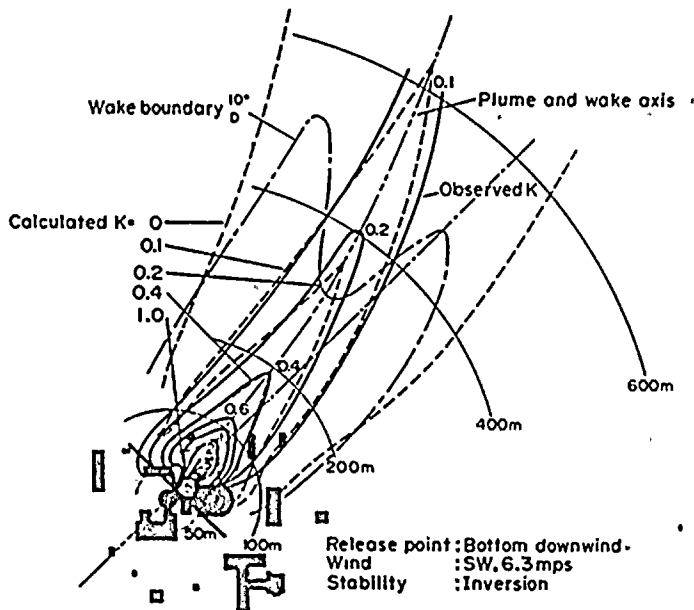

Fig. 13. K-Isopleths in the Ground Plane as Observed (Mean of Inversion Tests) and Calculated for Neutral Stability (Source: Dickson *et al.*, 1969).

6.3 Dispersion Model

The mathematical dispersion model that provided the best fit to the observation was of the following form:

$$X = 2F_m Q (\sigma_y \sigma_z \bar{u})^{-1} f(y) g(z) \tag{23}$$

where

X = concentration at point x, y, z

Q = release rate of source at ground level

σ_y = standard deviation of concentration distribution in y direction

σ_z = standard deviation of concentration distribution in z direction

$\bar{u}$ = local mean velocity at distance x, constant over y-z plane

$f(y)$ = distribution function in y direction

$g(z)$ = distribution function in z direction

2 = ground reflection factor

F_m = mass balance constant.

Explicit forms for σ_y, σ_z, $\bar{u}$, $f(y)$ and $g(z)$ were derived from the observations and introduced into Eq. 23, and M was then found from the mass balance equation F_m

$$Q = \int_{0x}^{\infty} \int_{-\infty}^{\infty} X\bar{u}\,dy\,dz \tag{24}$$

6.3.1 Plume Boundaries

In order to find σ_y, σ_z, $f(y)$ and $g(z)$ it was necessary to assume a form for the plume boundaries y_b and z_b.

Since the material was released in the cavity of the containment vessel, a form was needed to provide initial dispersion to the cavity boundary at $x = 0$ and subsequent growth by atmospheric turbulence at $x > 0$. The selected lateral and vertical boundary equations were

$$y_b = PW/2 + 2.5\,a_y x^{P_y} \tag{25}$$

$$z_b = H + 2.5\,a_z x^{P_z} \tag{26}$$

where

y_b, z_b = distance from plume axis to plume boundary

W = equivalent flat plate width (166 m)

H = equivalent flat plate height above ground (23 m)

a, p = constants for parabolic boundary expansion

P = building separation factor (0.75).

The terms $PW/2$ and H provide an initial plume boundary expansion due to cavity mixing. In the vertical direction, the expansion is allowed to go to the top edge of the equivalent flat plate. In the lateral direction, the constant P restricts the mixing to some fraction of the plate width. The physical rationale for P is to provide for interruption of cavity mixing by air seepage between buildings. The numerical value

of $P = 0.75$ was selected to provide a boundary half-width at $x = 0$ that would be consistent with the observed values of σ_y at $x > 0$ in neutral stability, as given in Fig. 9a.

The constants a_y, p_y, a_z and p_z were found by fitting the expression

$$\sigma = a x^P \tag{27}$$

to the C, D, E and F stability curves in open terrain in Fig. 9a, at $x = 200$ and $600\,m$. Numerical values of the constants are given in Table 3. The factor of 2.5 in Eqs. 25 and 26 implies that dispersion in an undisturbed atmosphere terminates at 2.5 σ.

The combination of initial expansion due to building wake plus subsequent growth by atmospheric turbulence, as given by Eqs. 25 and 26, is believed to adequately represent the actual plume boundary growth since the plume boundary lies near or outside of the wake boundary (see Figs. 12 and 13).

6.3.2 Distribution Functions

Equations for the growth of σ_y and σ_z with x can be found from the plume boundary equations if the form of the distribution functions $f(y)$ and $g(z)$ is known.

The lateral distribution function $f(y)$ was derived by measuring the lateral displacement of the K isopleths from the plume centerline in Figs. 12 and 13 at various downwind distances, and plotting them in non-dimensional form K/K_a vs y/y_b as in Fig. 14. The plume axis was assumed to be the (curved) line joining the ends of the K isopleth loops. The traverses were located at the ends of the isopleth loops. The small circles in Fig. 14 are the averages of left and right displacements. The values of y_b used in normalization were calculated from Eq. 25 in D stability.

The heavy curves in Fig. 14 are a Gaussian distribution and a parabolic distribution having the following equations:

Gaussian:

$$K/K_a = \exp[-y^2/2\sigma_y^2] \text{ with } \sigma_y = 0.4 y_b \tag{28}$$

Parabolic:

$$K/K_a = [1 - y/y_b]^2. \tag{29}$$

The observed distribution is clearly not Gaussian, and the parabolic form is a representative average fit to both sets of data.

The value of σ_y for the parabolic distribution is found by

$$\sigma_y^2 = \frac{\int_0^1 (K/K_a)(y/y_b)^2\, d(y/y_b)}{\int_0^1 (K/K_a)\, d(y/y_b)} \tag{30}$$

Substitution of K/K_a from Eq. 29 into Eq. 30 yields

$$\sigma_y = y_b/\sqrt{10} \quad \text{(parabolic distribution).} \tag{31}$$

Values of σ_y calculated by Eqs. (25) and (31) for C, D and E stability are plotted in Fig. 9a. The D curve is seen to lie between the lapse and inversion
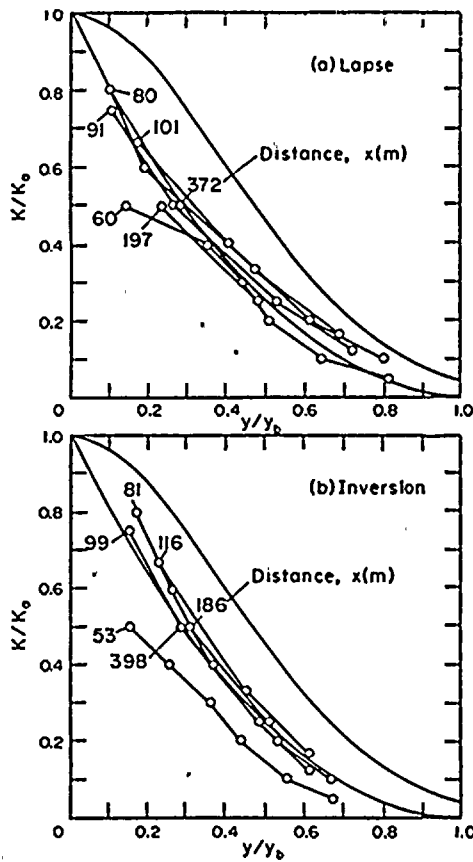
Fig. 14. Lateral Distribution of Normalized Concentration Coefficient. Top: Mean of Lapse tests. Bottom: Mean of Inversion Tests.

observations. The C and E curves are higher, following the site characteristics.

It is not possible to perform a similar analysis in the vertical since no data were taken in this direction. A Gaussian distribution was assumed because flow interruptions caused by building separation in the horizontal direction are not present in a vertical direction. Therefore σ_z is given by

$$\sigma_z = z_b/2.5 \quad \text{(Gaussian distribution).} \quad (32)$$

Values of σ_z calculated by Eqs. 26 and 32 are plotted in Fig. 9b. The calculated values are higher than the observed values. However it should be remembered that the observed values were, in fact, not observed but calculated from an assumed Gaussian distribution, and therefore do not provide a clear test of Eq. 32.

6.3.3 Dispersion Equation

In view of the above, the distributions used in Eq. 23 became

$$f(y) = (1 - y/\sqrt{10}\,\sigma_y)^2 \quad (33)$$

$$f(z) = \exp[-y^2/2\,\sigma_y^2] \quad (34)$$

and the standard deviations became

$$\sigma_y = 19.69 + a_y x^{p_y} \quad (35)$$

$$\sigma_z = 9.20 + a_z x^{p_z}. \quad (36)$$

The local mean velocity $\bar{u}$ was assumed to be that at the plate axis, given by Eq. 8, or

$$\bar{u}/\bar{u}_o = (1 - 8.16 x^{-2/3}). \quad (8)$$

Introduction of Eqs. 8 and 33–36 into Eqs. 23 and 24 yielded

$$F_m = 3/2 \sqrt{20}\,\pi. \quad (37)$$

For convenience in comparing the model predictions with observations. Eq. 23 was normalized according to Eq. 20 to yield the dispersion equation

$$K = \frac{AX\bar{u}_o}{Q} = 251.68\,(\sigma_y\sigma_z\bar{u}/\bar{u}_o)^{-1}\,f(y)\,g(z) \quad (38)$$

6.4 Comparison with Observations

Isopleths of K in the ground plane, calculated by Eq. 38, are shown in Figs. 12 and 13. The isopleths were made symmetrical about the curved plume axis. The wake boundary in D stability is also shown for reference. Agreement between calculated and observed K isopleths is good. There appears to be little difference between the lapse and inversion tests. Dispersion is controlled by wake turbulence for distances up to about 400 m and by atmospheric turbulence thereafter. This suggests that the parabolic distribution used for $f(y)$ in the wake region should be gradually replaced by the asymptotic Gaussian form at larger distances.

The variation of K along the plume axis is shown in Fig. 15. The lapse and inversion data points were
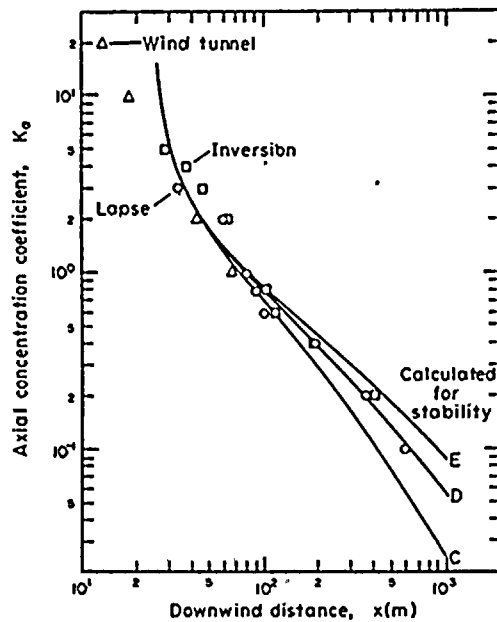

Fig. 15. Variation of Concentration Coefficient with Distance along Plume Axis.

measured at the ends of the K isopleth loops in Figs. 12 and 13. The wind tunnel data points were measured in a similar manner from Fig. 16. The curves marked C, D and E were calculated ,by Eq. 38. The D (neutral stability) curve is a good fit to the data for $x > 80$ m. Some scatter in the observations occurs in the range $30 < x < 80$ m. Eq. 38 deviates markedly from the observations at $x < 30$ m. This is a consequence of the assumed $\bar{u}/\bar{u}_o$ variation which goes to zero at $x = 23.3$ m and produces infinite K_o at the same distance.

The wind tunnel test data points merge smoothly with the field data points in the region of overlap. This lends credibility to the wind tunnel values at short downwind distances. Evidently a cavity diffusion model is needed to predict the observed values at short distances on physical grounds. Such a model is beyond the scope of this paper.

It is of some interest to assess the sensitivity of Eq. 38 to perturbations of the parameters. If σ_y, σ_z and $\bar{u}$ are unchanged, but $f(y)$ is changed from the parabolic to the Gaussian form, the calculated K values will be reduced by a factor of 0.84. Similarly, if the Gaussian form of $g(z)$ is replaced by the parabolic form, the multiplying factor for K is 1.19. If $\bar{u}$ is held constant and equal to $\bar{u}_o$, the factor changes with distance, as shown in Fig. 17.

It is also of some interest to compare Eq. 38 with the dispersion model of U.S.A.E.C. (1974) for calculating concentrations downwind of a leak in a containment structure. The governing equation for centerline concentration at ground level is

$$K_a = X A \bar{u}_o / Q = [\pi \sigma_y \sigma_z / A + c]^{-1} \tag{39}$$

where $c = 0.5$ and the other terms are as previously defined, together with the restriction that K_a may not be smaller than one-third of the value obtained by Eq. 39 with $c = 0$. Fig. 17 shows this model
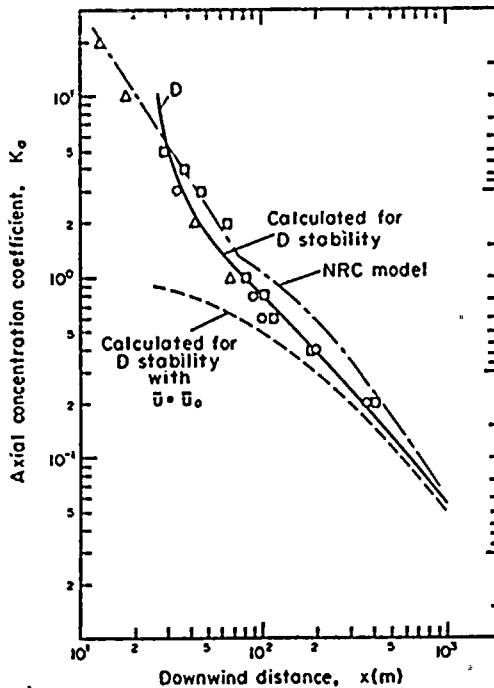

Fig. 17. Comparison of Dispersion Models.

for the EBR-II complex. The model is very good at close range but overestimates concentrations for $80 < x < 600$ m. The latter occurs because insufficient weight is given to initial broadening of the plume by the combined wake of all the buildings in the complex. At larger distances, initial building effects become less significant, and the differences between the N R C and equivalent flat plate models remains essentially in the lateral distribution function $f(y)$. As noted previously an asymptotic transformation to the Gaussian form is to be expected on physical grounds. Experimental data are needed to determine the rate at which this transformation should be introduced.

7. SUMMARY

The mean velocity and turbulence measured along a longitudinal axis downwind of the EBR-II reactor containment structure can be modeled by equations that were derived from measurements along the longitudinal axis of a suspended flat plate, with a modification to incorporate the effect of a solid ground boundary.

The parameter that is needed to quantify the model for the EBR-II complex is the size and shape of an equivalent flat plate to replace the assortment of buildings in the complex. It was found that a rectangular plate of height 46 m and width 166 m, half-imbedded in the ground at the lee surface of the containment vessel, was appropriate. The height dimension was selected as a visual average of the building heights. The width dimension was arrived at by trial and error, and seems to be physically reasonable in retrospect.

Fig. 16. K-Isopleths in the Ground Plane as Observed in Wind Tunnel Model Tests.
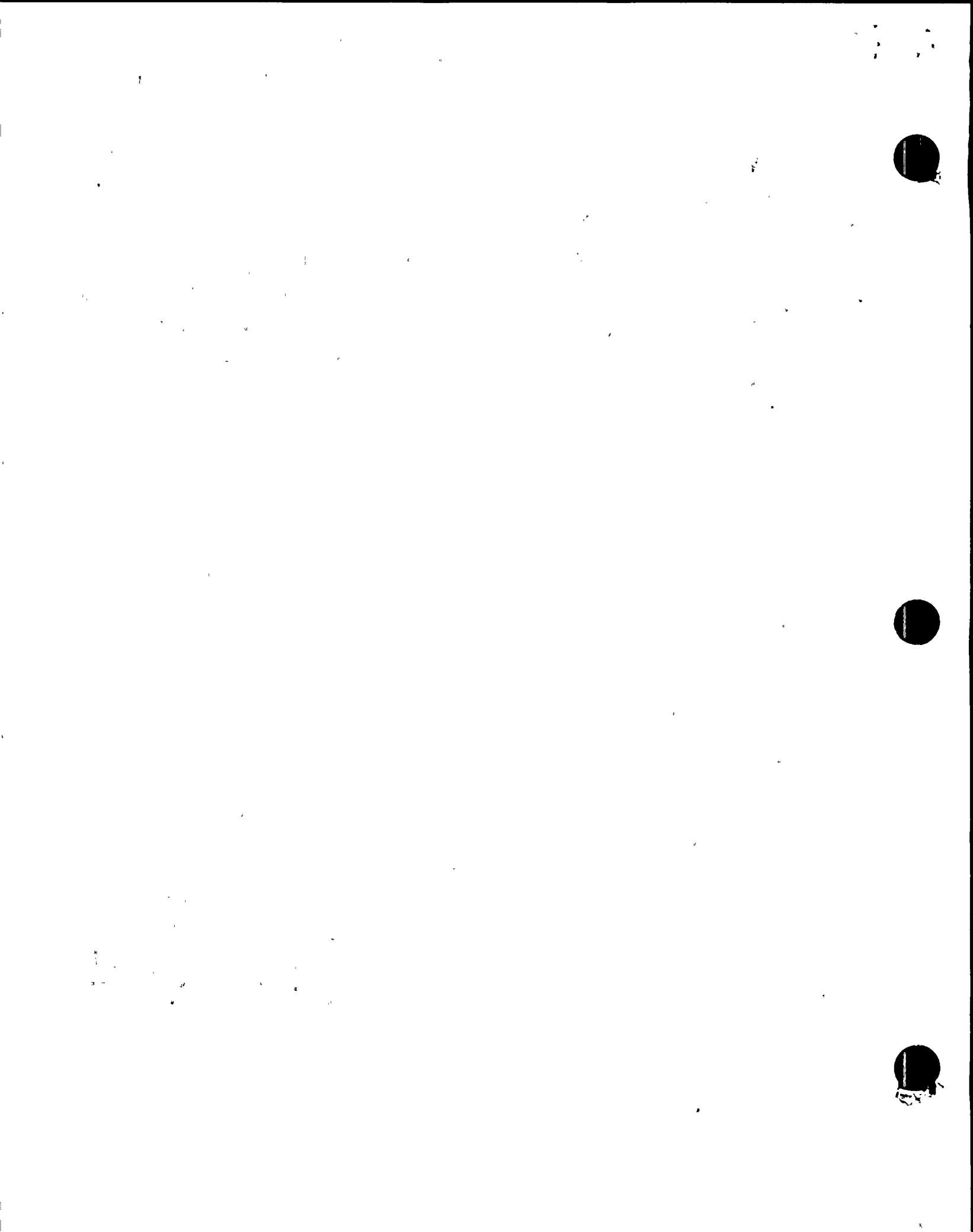
The ground boundary effect was introduced by multiplying the vertical component of turbulence intensity and the vertical height of the wake boundary by a factor of 0.52, which is the average value of σ_z/σ_y for point source dispersion over the test distance range in Pasquill D stability.

If the wake boundary is defined as the imaginary surface enclosing the region in which turbulence intensity is greater than atmospheric, then real wakes are finite in length, width and height, and the dimensions are inversely proportional to the atmospheric turbulence intensity components in the respective directions. The EBR-II complex wake was about 400 m long, 270 m wide and 70 m high, according to model predictions, under the neutral stability conditions that existed during the field tests.

The existence of a wake cavity at the EBR-II complex was indicated by the decrease of mean velocity and increase of turbulence intensity along the wake axis, with decreasing longitudinal distance. Extrapolation of this trend to zero mean velocity at $x = 23$ m suggests the termination of a cavity near that point. This is shorter than the cavity of the isolated EBR-II containment structure, and it indicates that flow irregularities created by wind passage between buildings may perturb individual building cavities.

The merging of individual cavities into a single composite cavity for the complex is indicated by the rapid initial dispersion of material to the lateral boundaries of the wake. However, insufficient information is available to define the shape of such a cavity or its internal flow dynamics.

A dispersion model was developed that included initial plume expansion governed by the equivalent flat plate dimensions, variation of mean velocity along the plume axis, parabolic distribution of material in the horizontal and Gaussian distribution in the vertical. The model was in good agreement with the field observations beyond a distance of 30 m, but it overpredicted at shorter distances. The failure of the model at short distances is due to inapplicability in a wake cavity region.

At distances longer than 600 m, the model is expected to overpredict axial concentrations by a maximum of 19% because flow reorganization after termination of the wake will eventually create a Gaussian, rather than parabolic, lateral distribution of concentration. The model can be modified to incorporate this transition, but information as to the rate of transition is lacking.

The dispersion model was tuned to the observed data in the following respects: selection of the equivalent flat platewidth W, selection of the building separation factor P, and selection of the parabolic distribution for lateral dispersion. It should be possible to formulate techniques for calculating these parameters from the geometry of the complex, but additional tests in other configurations are needed to provide the requisite data base. Meanwhile, the results of this investigation may serve as a guide for making preliminary estimates of the parameters in other applications.

REFERENCES

Castro, I. P., and A. G. Robins (1975): The effect of a thick incident boundary layer on the flow around a small surface mounted cube. Central Electricity Generating Board, Marchwood Laboratories Report R/M/N795, Marchwood, England.

Cooper R. D., and M. Lutzky (1955): Exploratory investigation of turbulent wakes behind bluff bodies, U.S. Navy Dept. David Taylor Model Basin Rep. No. DTMB-963.

Counihan, J., J. C. R. Hunt and P. S. Jackson (1974): Wakes behind two-dimensional surface obstacles in turbulent boundary layers. *J. Fluid Mech.* 3 564, pp 529–563.

Dickson, C. R., G. E. Start and E. H. Markee, Jr. (1969): Aerodynamic effects of the EBR-II reactor complex on effluent concentrations. Nuclear Safety, 10, No. 3 May–June.

Fail, R., J. A. Lawford and R. C. W. Eyre (1957): Low speed experiments on the wake characteristics of flat plates normal to an air stream. Aer. Res. Council R and M 3120. London.

Halitsky J., J. Golden, P. Halpern, and P. Wu (1963): Wind tunnel tests of gas diffusion from a leak in the shell of a nuclear power reactor and from a nearby stack., New York University Dept. of Met. and Ocean. GSL Rep. No. 63-2 (Contract Cwb-10321 with U.S. Weather Bureau Environmental Meteorological Research Project).

Slade, D. H., ed. (1968): Meteorology and Atomic Energy, U.S. Atomic Energy Commission Div. of Tech. Inf. CFSTI Doc. TID-24190.

U.S.A.E.C. (1974): Regulatory Guide 1.4, Rev. 2, Assumptions Used for Evaluating the Potential Radiological Consequences of a Loss of Coolant Accident for Boiling Water Reactors.

Van der Hoven I., ed. (1967): Atmospheric Transport and Diffusion in the Planetary Boundary Layer, U.S. Dept. of Commerce, ESSA Air Resources Laboratories Tech. Mem. RLTM-ARL 3, Dec. 1967.

Van der Hoven I., ed. (1968): Atmospheric Transport and Diffusion in the Planetary Boundary Layer, U.S. Dept. of Commerce, ESSA Air Resources Laboratories Tech. Mem. ERLTM-ARL 5, May 1968.

APPENDIX A

Derivation of Gaussian CIC equations

To obtain σ_y

Let

$$X_{z=0} = Q(\pi\sigma_y\sigma_z\bar{u})^{-1} \exp\{-y^2(2\sigma_y^2)^{-1}\} \qquad \text{A.1}$$

Then

$$\text{CIC} = \int_{-\infty}^{\infty} X_{z=0}\, dy = Q(\pi\sigma_y\sigma_z\bar{u})^{-1}(2\pi)^{1/2}\sigma_y \qquad \text{A.2}$$

and

$$X_p = X_{y=z=0} = Q(\pi\sigma_y\sigma_z\bar{u})^{-1} \qquad \text{A.3}$$

Combine A.2 and A.3 to obtain:

$$\sigma_y = (\text{CIC})(2\pi)^{-1/2} X_p^{-1} \qquad \text{A.4}$$

To obtain σ_z

$\qquad\qquad\qquad\qquad\qquad\qquad\qquad\qquad\qquad\qquad = (CIC)(2\pi)^{1\,2}\,\sigma_z \qquad\qquad\qquad A.6$

Let

Then

$$Q = \int_{-\infty}^{\infty} \int_{-\infty}^{\infty} X\bar{u}\,dy\,dz \qquad\qquad A.5 \qquad\qquad \sigma_z = Q(CIC)^{-1}(2\pi)^{-1/2} \qquad A.7$$

$$= \int_{-\infty}^{\infty} X_{z=0}\,dy \int_{-\infty}^{\infty} \exp\left\{-z^2(2\sigma_z^2)^{-1}\right\}\,dz$$